

A Vertical Diffusion Scheme to estimate the atmospheric rectifier effect

Baozhang Chen and Jing M. Chen

Department of Geography and Program in Planning, University of Toronto, Toronto, Ontario, Canada

Jane Liu

Department of Physics, University of Toronto, Toronto, Ontario, Canada

Douglas Chan, Kaz Higuchi, and Alexander Shashkov

Air Quality Research Branch, Meteorological Service of Canada, Toronto, Ontario, Canada

Received 27 June 2003; revised 13 October 2003; accepted 6 November 2003; published 21 February 2004.

[1] The magnitude and spatial distribution of the carbon sink in the extratropical Northern Hemisphere remain uncertain in spite of much progress made in recent decades. Vertical CO₂ diffusion in the planetary boundary layer (PBL) is an integral part of atmospheric CO₂ transport and is important in understanding the global CO₂ distribution pattern, in particular, the rectifier effect on the distribution [Keeling *et al.*, 1989; Denning *et al.*, 1995]. Attempts to constrain carbon fluxes using surface measurements and inversion models are limited by large uncertainties in this effect governed by different processes. In this study, we developed a Vertical Diffusion Scheme (VDS) to investigate the vertical CO₂ transport in the PBL and to evaluate CO₂ vertical rectification. The VDS was driven by the net ecosystem carbon flux and the surface sensible heat flux, simulated using the Boreal Ecosystem Productivity Simulator (BEPS) and a land surface scheme. The VDS model was validated against half-hourly CO₂ concentration measurements at 20 m and 40 m heights above a boreal forest, at Fraserdale (49°52'29.9"N, 81°34'12.3"W), Ontario, Canada. The amplitude and phase of the diurnal/seasonal cycles of simulated CO₂ concentration during the growing season agreed closely with the measurements (linear correlation coefficient (R) equals 0.81). Simulated vertical and temporal distribution patterns of CO₂ concentration were comparable to those measured at the North Carolina tower. The rectifier effect, in terms of an annual-mean vertical gradient of CO₂ concentration in the atmosphere that decreases from the surface to the top of PBL, was found at Fraserdale to be about 3.56 ppmv. Positive covariance between the seasonal cycles of plant growth and PBL vertical diffusion was responsible for about 75% of the effect, and the rest was caused by covariance between their diurnal cycles. The rectifier effect exhibited strong seasonal variations, and the contribution from the diurnal cycle was mostly confined to the surface layer (less than 300 m).

INDEX TERMS: 0315 Atmospheric Composition and Structure: Biosphere/atmosphere interactions; 0343 Atmospheric Composition and Structure: Planetary atmospheres (5405, 5407, 5409, 5704, 5705, 5707); 1615 Global Change: Biogeochemical processes (4805); 1060 Geochemistry: Planetary geochemistry (5405, 5410, 5704, 5709, 6005, 6008); **KEYWORDS:** vertical CO₂ diffusion, atmospheric rectifier effect, planetary boundary layer, boreal forest, Fraserdale

Citation: Chen, B., J. M. Chen, J. Liu, D. Chan, K. Higuchi, and A. Shashkov (2004), A Vertical Diffusion Scheme to estimate the atmospheric rectifier effect, *J. Geophys. Res.*, 109, D04306, doi:10.1029/2003JD003925.

1. Introduction

[2] Because of the complexity of the Earth's climate system, the sources and sinks of carbon to and from the atmosphere remain uncertain despite much progress in recent decades [Schimel *et al.*, 2001]. Global carbon budgets have been updated in the most recent IPCC assessment, and IPCC recognized that an improved understanding of the

CO₂ cycle is essential to predicting the future rate of atmospheric CO₂ increase and formulating an international CO₂ management strategy [Prentice *et al.*, 2001]. Over the past 2 decades, accumulated evidence indicates that contributions of the extratropical Northern Hemisphere land areas to the global uptake of anthropogenic CO₂ is significant [Schimel *et al.*, 2001], though there still exists a wide range of estimates of terrestrial sinks in these areas from -0.6 to -2.3 Gt C yr⁻¹ in the 1980s [Heimann, 2001]. These estimates were obtained from a number of different approaches, such as analysis of land inventory data [Brown,

1996; Brown and Schroeder, 1999; Spiecker et al., 1996; Pacala et al., 2001; Kurz and Apps, 1999], combining transport models and atmospheric CO₂ observations [Gurney, 2002; Enting et al., 1995; Fan et al., 1998; Kaminski et al., 1999; Bousquet et al., 1999, 2000; Baker, 2000; Taguchi, 2000; Rayner et al., 1999; Tans et al., 1990; Heimann, 2001], atmospheric O₂ data [Battle et al., 2000; Bender et al., 1996; Keeling et al., 1996; Rayner et al., 1999], isotopic analysis [Battle et al., 2000; Rayner et al., 1999; Ciatis et al., 1995], studies of land-use change [Houghton et al., 1999], and ecosystem process models [Schimel et al., 2000; McGuire, 2001; Running et al., 1999; Denning et al., 1996a]. Overall, these approaches can be divided into two primary groups: (1) atmospheric-based methods (the tracer-transport inversion method) and (2) land-based approaches incorporating direct inventories of carbon on the ground and ecosystem models [e.g., Pacala et al., 2001].

[3] In nature, the carbon budget must satisfy all the observational constraints simultaneously, including the rate of change of the concentration and isotopic composition of atmospheric CO₂, the north-south gradient in annual mean concentration, the amplitude of the seasonal cycle and its variation with latitude [Denning et al., 1996b]. However, in practice, this is almost never the case [Denning et al., 1999]. Atmospheric-based studies typically depend much more on the time-averaged data at remote marine surface locations, but do not adequately use ecosystem data [Bousquet et al., 1999]. By contrast, land-based approaches which attempt to diagnose fluxes from meteorological, vegetation and soil conditions based on ecological principles [Dixon et al., 1990; Potter et al., 1993] typically ignore the atmospheric constraints, except as needed for validation [Denning et al., 1996b]. One possible way to reduce the large uncertainties is to combine these two existing approaches through a careful selection of constraints.

[4] Information on the temporal and spatial variability in CO₂ concentration may be used as constraints to models. Temporal covariance between the terrestrial surface CO₂ flux and the atmospheric transport/mixing of CO₂ through the planetary boundary layer (PBL) produces vertical and horizontal CO₂ gradients [Denning et al., 1995, 1996b; Stephens et al., 2000]. During summer over continents, vertical mixing of CO₂ is vigorous and the PBL is relatively deep. The photosynthesis signal is diluted through deep mixing; meanwhile the low-CO₂ air is transported into upper troposphere [e.g., Bakwin et al., 1998]. In contrast, during fall and winter the PBL is shallow; the respiration signal is trapped near the surface. This process produces the annual mean profile with higher CO₂ concentrations at the surface and lower concentrations aloft over land [Denning et al., 1996b].

[5] This and other similar processes (e.g., diurnal variations) have been termed “rectifier” effects [Keeling et al., 1989; Denning et al., 1995], by analogy to an electronic rectifier produced by a diode with truncated minima when converting an alternating current to a direct current. The atmospheric rectifier effect can be defined as any temporal covariation (e.g., seasonal and diurnal, etc.) between the surface flux and atmospheric mixing or transport that produces a time-mean spatial concentration gradient of a

specified trace gas in the atmosphere [Denning et al., 1995; Stephens et al., 2000]. This broad definition includes both vertical and horizontal (terrestrial and marine-land) rectifiers of CO₂, CO, O₂, and other tracers at any temporal scale (seasonal and diurnal) [Pearman and Hyson, 1980; Denning et al., 1995, 1996b, 1999; Stephens et al., 1998; Stephens, 1999], and also includes the isotope-ratio rectifiers corresponding to these terrestrial-concentration effects [Stephens et al., 2000]. Here, we are only concerned with the vertical CO₂ rectifier effect including the seasonal and diurnal rectifiers, which we will refer to simply as the seasonal and diurnal rectifier effects in this paper. The global redistribution of CO₂ due to the rectifier effect has been investigated by Denning et al. [1995, 1996b]. The primary results of TransCom 3 [Gurney, 2002] also indicated that the rectifier effect appears to be responsible for much of the discrepancy in estimated magnitude and spatial distribution of carbon uptake in the extratropical Northern Hemisphere. One possible way to reduce these uncertainties in the size and spatial distribution of the extratropical Northern Hemisphere carbon sink is to estimate the strength of atmospheric rectification at different terrestrial ecosystems over these regions.

[6] The rectifier effect occurs mostly due to the control of the planetary boundary layer on the vertical transport of energy and mass. Thus, a one-dimensional (1-D) vertical modeling scheme would be an essential step in quantitative description of the rectifier effect. For this purpose, a Vertical Diffusion Scheme (VDS) based on turbulent transfer of scalars has been developed in the present study to investigate the vertical CO₂ diffusion processes and the atmospheric rectifier effect in the planetary boundary layer.

[7] In order to estimate the heat flux, which affects the mixed layer development, the complete surface energy budget was simulated using a recently developed land surface scheme, named EASS (Ecosystem-Atmosphere Simulation Scheme). Evaluation of a regional carbon budget by comparing simulated and observed CO₂ concentrations requires simulation of terrestrial ecosystem metabolism. The VDS was driven by the net ecosystem carbon flux simulated using the Boreal Ecosystem Productivity Simulator (BEPS) [Chen et al., 1999; Liu et al., 1999, 2002] coupled to EASS in this study. The EASS model and the integrated EASS-BEPS model will be reported elsewhere. In the present paper, we focus on the one-dimensional CO₂ vertical transfer model (VDS) involving the interaction between plant canopies and the atmosphere in the surface layer and the dynamics of the mixed layer. In addition, we perform a model experiment, in which the CO₂ flux derived by BEPS was prescribed without a diurnal cycle (e.g., using daily/monthly mean values) to investigate the impact of the diurnal cycle on the rectifier effect.

[8] The purposes of this paper are: (1) to describe the VDS model, (2) to validate the model against CO₂ concentration measurements at 20 m and 40 m heights above a boreal forest, and (3) to simulate vertical CO₂ profiles at different temporal scales (diurnal, monthly, and seasonal) and to estimate the atmospheric rectifier effect using the verified VDS model at the same location. In section 2, an integrated modeling system involving energy balance of the surface and the vertical transport is introduced, and then the VDS model is described in

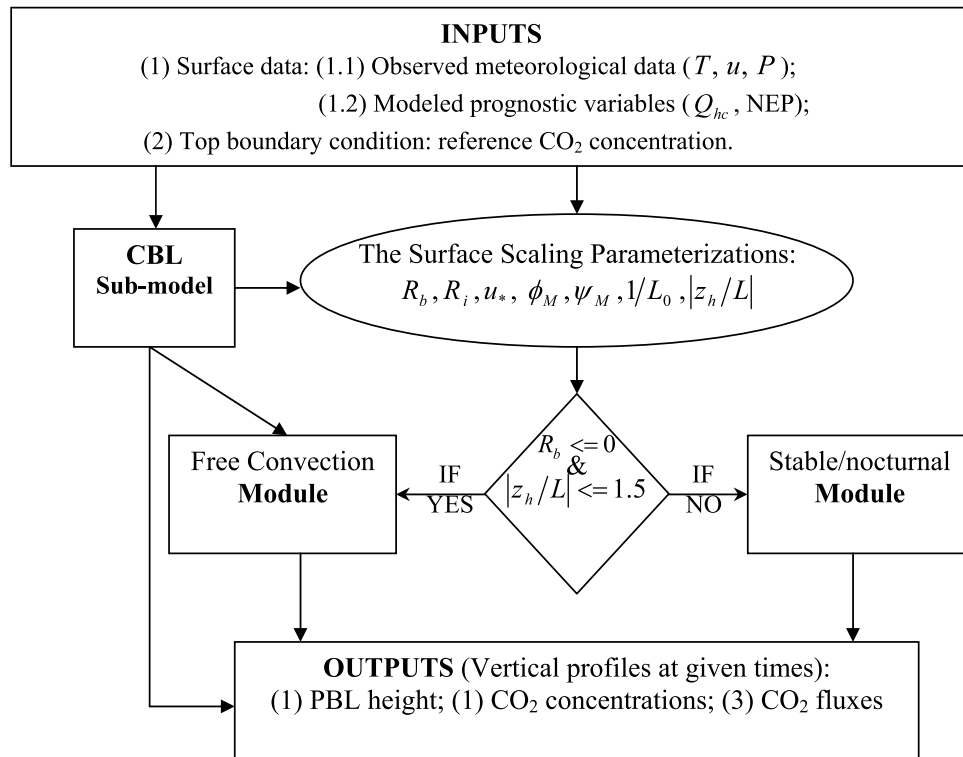


Figure 1. Schematic structure of the VDS model (T is air temperature, u is wind speed, P is the air pressure, Q_{hc} is the land surface sensible heat flux at the canopy level, NEP is net ecosystem productivity, R_b is the bulk Richardson number, R_i is the gradient Richardson number, u_* is the friction wind, ϕ_M is the dimensionless wind shear in the surface layer, Ψ_M is the surface layer stability correction term for momentum, L is the Monin Obukhov length, L_0 is the Monin Obukhov length in the surface layer, and z_h is the CBL height. The two modeled prognostic variables (Q_{hc} , NEP) are calculated using EASS and BEPS, respectively).

detail. In section 3, simulated diurnal and seasonal series of CO₂ concentrations and their vertical profiles are analyzed and compared to observations.

2. Model Description

2.1. Introduction to the VDS Model

[9] The carbon cycle involving soil, vegetation, and atmosphere and driven by solar and thermal energy is simulated using an integrated modeling system. This system consists of three components, the Vertical Diffusion Scheme (VDS), the Ecosystem-Atmosphere Simulation Scheme (EASS), and the Boreal Ecosystem Productivity Simulator (BEPS). The three components are linked through two prognostic variables: land surface sensible heat fluxes (Q_{hc}) affecting the mixed layer development, and net ecosystem productivity (NEP) driving vertical CO₂ transfer, which are calculated using EASS and BEPS, respectively, at each computing time step. The VDS is designed to simulate scalar diffusion processes in the planetary boundary layer (PBL). These processes modify the lowest 100 to 3000 m of the atmosphere, though the troposphere extends from the ground up to an average of 11 km [Stull, 1993]. The maximum top boundary height in VDS is 2520 m. Generally, over the land surface under a high-pressure weather system the PBL has a well-defined structure that evolves in a diurnal cycle [Stull, 1993]. The

four major components of this structure are the surface layer, the stable boundary layer, the convective boundary layer, and the residual layer. Many researchers use second-order closure or higher-order closure methods to study/simulate the complex diurnal evolutions of the PBL at the expense of high computation power. First-order closure is often called the gradient transport theory or well-known K-theory. Although it is one of the simplest parameterization schemes, it is only applicable in situations dominated by small-eddy. Unfortunately, it frequently fails when large eddies are present. Furthermore, in the real atmosphere, there are occasions where transport occurs against the gradient (i.e., counter gradient) [Stull, 1993]. Thus, K-theory is not applicable for use in convective mixed layers. Hence to minimize the problem, we selected different schemes to treat different situations of the PBL structure. One is a stable/nocturnal module in which K-theory is used; another is a free-convection module which is based on Estoque's principles [Esoque, 1968; Blackadar, 1976, 1978]. The criteria that determine which module is applicable, as shown in Figure 1, are the sign and magnitude of the bulk Richardson number R_b in the surface layer and the magnitude of $|z_h/L|$ [Zhang and Anthes, 1982]. Here z_h denotes the height of the mixed layer and L is the Monin-Obukhov length.

[10] The VDS model is integrated with the surface fluxes calculated using coupled BEPS-EASS at 1-min

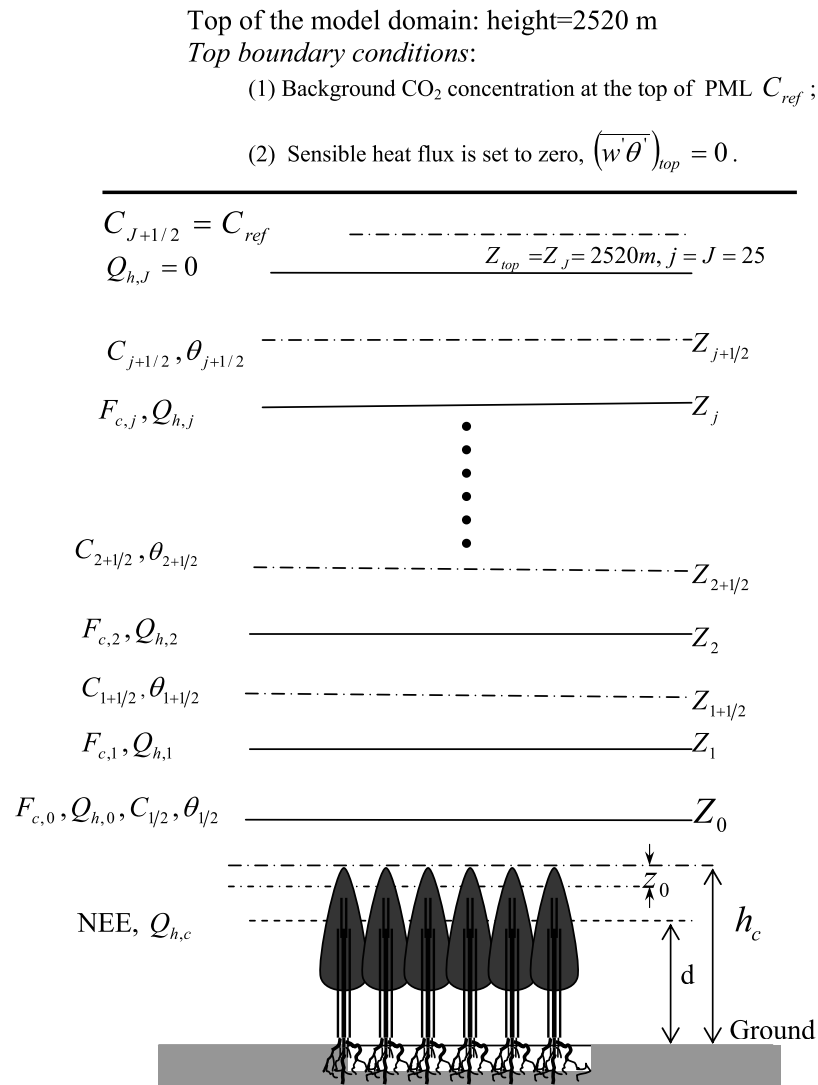


Figure 2. Schematic vertical structure of the VDS model domain (h_c is the height of the vegetation canopy, d is the displacement height, z_0 is the roughness length, C is the CO₂ concentration, θ is the potential temperature of air; F is the CO₂ flux; and Q_h is the sensible heat flux. The subscripts “0” and “1/2” denotes the lower surface layer for the CO₂ flux and the sensible heat flux, and for the CO₂ concentration and the potential temperature of air, respectively. Here j is each layer with a vertical separation of 100 m, J - is the top of model domain (= 25)). See color version of this figure at back of this issue.

computing time steps. This model includes four major components: the surface scaling parameterizations, convective boundary layer (CBL) sub-model, stable/nocturnal module, and free convection module (Figure 1). The surface scaling parameters including the bulk Richardson number (R_b), the gradient Richardson number (Ri), the Obukhov length in the surface layer (L_0), the dimensionless wind shear in the surface layer (ϕ_M), and the surface layer stability correction term for momentum (Ψ_M), are calculated using the general equations cited from Stull [1993] (equation 5.6.3 for R_b , equation 5.6.2 for Ri , equation 5.7c for L_0 , equation 9.7.5a, b, c for ϕ_M and equation 9.7.5h, i for Ψ_M). The diurnal evolution of the CBL is modeled in the CBL submodel (Figure A1, Appendix A). The vertical structure of the VDS model domain is described in section 2.1. The stable/nocturnal

module and free convection module are introduced in sections 2.2 and 2.3. The model boundary conditions, initialization and computational procedures are discussed in sections 2.4 and 2.5, respectively.

2.2. Vertical Structure of the VDS Model Domain

[11] The vertical structure of the model is illustrated in Figure 2. Here h_c is the height of the vegetation canopy, d is the displacement height estimated as $0.67 \cdot h_c$, and z_0 is the roughness length = $0.1 \cdot h_c$. The lower surface layer (Z_0) in this model is set to a fixed depth of 20 m and the levels above are placed with a vertical separation of 100 m, which is suitable for 60 s time step used in the presented VDS model computation (smaller separation requires smaller time step). For convenience, we use the subscript “s” to denote the lower surface layer (i.e., Z_0 ,

$F_{c,0}$, $Q_{h,0}$, $C_{1/2}$ and $\theta_{1/2}$ as Z_s , $F_{c,s}$, $Q_{h,s}$, C_s and θ_s , respectively).

[12] For convenience of computation, all the prognostic variables (C and θ denote CO₂ concentration and potential temperature of air, respectively) are defined at the $Z_{j+1/2}$ levels, and all the diagnostic quantities, such as Richardson number R_i , the eddy exchange coefficient K , and the fluxes of CO₂, sensible heat flux, are defined at Z_j level.

2.3. Stable/Nocturnal Module

[13] For the stable/nocturnal module, in which the atmosphere is usually stable or at most marginally unstable and no large eddies are present in the flow, a first-order closure scheme (K -theory) is used. There has been no lack of creativity by investigators in designing parameterization schemes for eddy-transfer coefficient K [Stull, 1993]. K varies as the turbulence varies. Thus K can be parameterized as a function of Richardson number (Appendix B).

[14] The following sets of equations are used to compute diagnostic variables (fluxes) and predictive quantities (potential temperature and CO₂ concentration),

[15] (1) Diagnostic variables (upward, positive)

$$Q_{h,j} = -K_{h,j} \rho c_p \frac{\theta_{j+1/2} - \theta_{j-1/2}}{Z_{j+1/2} - Z_{j-1/2}} (j = 1, \dots, 24), \quad (1a)$$

$$F_{c,j} = -K_{c,j} \frac{C_{j+1/2} - C_{j-1/2}}{Z_{j+1/2} - Z_{j-1/2}} (j = 1, \dots, 25), \quad (1b)$$

[16] (2) Predictive quantities,

$$\frac{\theta_{j-1/2,t+\Delta t} - \theta_{j-1/2,t}}{\Delta t} = -\frac{1}{\rho c_p} \frac{Q_{h,j} - Q_{h,j-1}}{Z_j - Z_{j-1}} (j = 1, \dots, 25), \quad (2a)$$

$$\frac{C_{j-1/2,t+\Delta t} - C_{j-1/2,t}}{\Delta t} = -\frac{F_{c,j} - F_{c,j-1}}{Z_j - Z_{j-1}} (j = 1, \dots, 25). \quad (2b)$$

In equations (1) and (2), Q_h and F_c are the upward sensible heat flux and the upward CO₂ flux at j level, respectively; θ and C denote the potential temperature and the CO₂ concentration at $j - 1/2$ level, respectively (Figure 2). Computing time step, $\Delta t = 60$ s. Model boundary conditions at the bottom (when $j = 1$, $Q_{h,0}$ and $F_{c,0}$) and at the top (when $j = 25$, $C_{25^{1/2}}$ and $Q_{h,25}$) will be discussed in section 2.4.

2.4. Free Convection Module

[17] On fair weather days, turbulent CBL begins to develop within around half an hour after sunrise depending on the solar heating on the ground. The resulting turbulence in the mixed layer is usually convectively driven and tends to mix heat, moisture, momentum, and CO₂ in the vertical direction. Having made the assumption that the turbulence in the mixed layer mixes the entire boundary layer from the surface up to the capping inversion, the CBL can be described as a single well-mixed layer in which certain

conserved quantities are independent of height [Driedonks and Duynkerke, 1989]. If we assign the total mass of air column in CBL as M , the fraction of exchanged mass caused by uplifting plumes from the lower surface layer per unit time as dM_1/dt , and the fraction of exchanged mass caused by entraining from the top of the mixed layer per unit time as dM_2/dt , the following equation can be formulated from energy and mass conservation,

$$M \frac{\partial \theta_m}{\partial t} = \frac{dM_1}{dt} (\theta_s - \theta_m) + \frac{dM_2}{dt} (\theta_t - \theta_m), \quad (3a)$$

$$M \frac{\partial C_m}{\partial t} = \frac{dM_1}{dt} (C_s - C_m) + \frac{dM_2}{dt} (C_t - C_m). \quad (3b)$$

where θ_s , θ_m and θ_t represent the potential temperature in the lower surface layer, in the mixed layer, and at the top of the mixed layer, respectively. C_s , C_m and C_t are the CO₂ concentration in the lower surface layer, in the mixed layer, and at the top of the mixed layer, respectively.

[18] We define β_{M_1} and β_{M_2} as the fractions of total mass exchange between the mixed layer and the lower surface layer per unit time and between the mixed layer and the top of the mixed layer per unit time, that is $\beta_{M_1} = M^{-1} dM_1/dt$ and $\beta_{M_2} = M^{-1} dM_2/dt$. Moreover, as shown in Figure A1, $\Delta\theta$, the change in potential temperature across the inversion layer, equals $\theta_t - \theta_m$. Therefore equations (3a) and (3b) can be rewritten, respectively, as,

$$\frac{\partial \theta_m}{\partial t} = \beta_{M_1} (\theta_s - \theta_m) + \beta_{M_2} \Delta\theta, \quad (4a)$$

$$\frac{\partial C_m}{\partial t} = \beta_{M_1} (C_s - C_m) + \beta_{M_2} (C_t - C_m). \quad (4b)$$

In our model, the CBL is divided into many layers with a vertical separation of 100 m (Figure 2). Based on the energy conservation principle, analogue to equation (4) of the whole CBL therefore the changes of prognostic variables for each layer above the lower surface layer are predicted by

$$\frac{\partial \theta_{j-1/2}}{\partial t} = \beta_{m_1} (\theta_s - \theta_{j-1/2}) + \beta_{m_2} \Delta\theta \quad (j \geq 2), \quad (5a)$$

$$\frac{\partial C_{j-1/2}}{\partial t} = \beta_{m_1} (C_s - C_{j-1/2}) + \beta_{m_2} (C_t - C_{j-1/2}) \quad (j \geq 2). \quad (5b)$$

where $\beta_{m_1} = m^{-1} \partial m_1/\partial t$, $\beta_{m_2} = m^{-1} \partial m_2/\partial t$, m denotes the total amount of air mass in each cell in a layer, and $\partial m_1/\partial t$ and $\partial m_2/\partial t$ represent the quantity of exchanged mass between the cell and the lower surface layer and between the cell and the top of the mixed layer per unit time, respectively.

[19] To determine the values of β_{m_1} and β_{m_2} , we assign β_m as the total of both β_{m_1} and β_{m_2} , that is,

$$\beta_m = \beta_{m_1} + \beta_{m_2}. \quad (6)$$

An expression for the heat flux at any level in the mixed layer given by *Blackadar* [1978] and *Westphal* [1981] is introduced here,

$$Q_h(z) = Q_{h,s} - \beta_m \rho c_p \int_{z_s}^z [(\theta_s - \theta(z))] dz. \quad (7)$$

As assumed in Appendix A, the heat flux at the top of entrainment zone (see Figure A1) equals zero; consequently, equation (7) can be rewritten as

$$Q_{h,s} = \beta_m \rho c_p \left(\int_{z_s}^{z_h} [(\theta_s - \theta(z))] dz + \int_{z_h}^{h_2} (\theta_s - \theta(z)) dz \right), \quad (8)$$

As discussed in Appendix A, the most negative heat flux (Q_{z_h}) occurs at the top of the convective mixed layer (z_h), and from equation (7), there is,

$$Q_{z_h} = Q_{h,s} - \beta_m \rho c_p \int_{z_s}^{z_h} (\theta_s - \theta(z)) dz. \quad (9)$$

Substituting equation (8) in equation (9) yields,

$$Q_{z_h} = \beta_m \rho c_p \int_{z_h}^{h_2} (\theta_s - \theta(z)) dz. \quad (10)$$

Combining equations (8) and (10) and equation (A4) (see Appendix A), we can derive,

$$\beta_m = Q_{h,s} \left[\rho c_p \frac{1}{1+c} \left(\int_{z_s}^{z_h} (\theta_s - \theta(z)) dz \right) \right]^{-1}, \quad (11)$$

where c is calculated from equation (A5).

[20] As mentioned above, the PBL is divided into many layers with a vertical separation of 100 m in our model (Figure 2), equation (11) can then be written in the discrete form as

$$\beta_m = \frac{(1+c)Q_{h,s}}{\rho c_p} \left(\sum_2^{J_{CBL}} (\theta_s - \theta_{j-1/2}) \Delta z \right)^{-1}, \quad (12)$$

where J_{CBL} is the maximum number of layers in the growing CBL, $J_{CBL} = \text{int}[z_h/\Delta z]$; z_h is derived from equation (A9), $\Delta z = 100$ m.

[21] Based on the energy and mass conservation principle, the exchange ratios of mass between the mixed layer and the surface layer (dM_1/dt) and between the mixed layer and the top of PBL (dM_1/dt) must be proportional to the heat flux at the surface layer ($Q_{h,s}$) and the top of the PBL layer (Q_{z_h}). Analogue to equation (A4), the relationship between β_{m_1} and β_{m_2} must be,

$$\beta_{m_2} = c\beta_{m_1}. \quad (13)$$

Combining equations (6), (12), and (13), we can solve for β_{m_1} and β_{m_2} as:

$$\beta_{m_1} = \frac{Q_{h,s}}{\rho c_p} \left(\sum_2^{J_{CBL}} (\theta_s - \theta_{j-1/2}) \Delta z \right)^{-1}, \quad (14a)$$

$$\beta_{m_2} = c \frac{Q_{h,s}}{\rho c_p} \left(\sum_2^{J_{CBL}} (\theta_s - \theta_{j-1/2}) \Delta z \right)^{-1}. \quad (14b)$$

[22] Similar to the principle of energy conservation demonstrated above, the principle of mass conservation can also be used to derive the following equation for estimating the rates of change in the CO₂ mixing ratio in the lower surface layer,

$$\frac{\partial C_s}{\partial t} = \left[F_{c,s} - \beta_{m_1} \sum_2^m (C_s - C_{j-1/2}) \Delta z \right] / (z_1 - d). \quad (15)$$

2.5. Boundary Conditions

[23] Both bottom and top boundary conditions are important and need to be selected carefully in one-dimensional models such as VDS. The bottom conditions of VDS are obtained from EASS and BEPS, while the top conditions are calculated using CO₂ concentration measurements at a site in the surface layer and weekly airborne flask measurements at a marine site of comparable latitude.

2.5.1. Bottom Boundary Conditions

[24] Upward fluxes of carbon and sensible heat from the lower surface layer (here at 20 m) into the PBL are the two bottom boundary conditions. Though these two fluxes (Q_{hc} , NEP) at the canopy displacement level are calculated from the integrated BEPS-EASS model, can they be treated as identical to those at the top of the lower surface layer? If so, considerable errors result, especially in the early morning when a strong laminar flow exists and the heat storage change in the lower atmosphere is considerable. Recent literature tends to confirm that the heat storage change in the surface layer is not negligible [Verma *et al.*, 1986; McMillen, 1988; Hollinger *et al.*, 1994; Lee, 1998; Lee *et al.*, 2001; Lee and Hu, 2002; Paw *et al.*, 2000; Yi *et al.*, 2000]. How to derive surface layer fluxes (20 m height) from those at canopy-level is discussed as follows.

[25] For our one-dimensional model by assuming no divergence of horizontal eddy flux and no horizontal advection and ignoring the molecular term, one can obtain equation (16) for net ecosystem exchange (NEE) of CO₂ from the conservation equation of a scalar C in the $x - z$ plane [Lee, 1998; Lee and Hu, 2002],

$$NEE = \int_{h_c}^{z_s} \frac{\partial \bar{C}}{\partial t} dz + (\overline{w' C'})_{z_s}, \quad (16)$$

where subscript z_s denotes the top of the surface layer and $\langle \bar{C} \rangle$ is the averaged concentration between the displacement

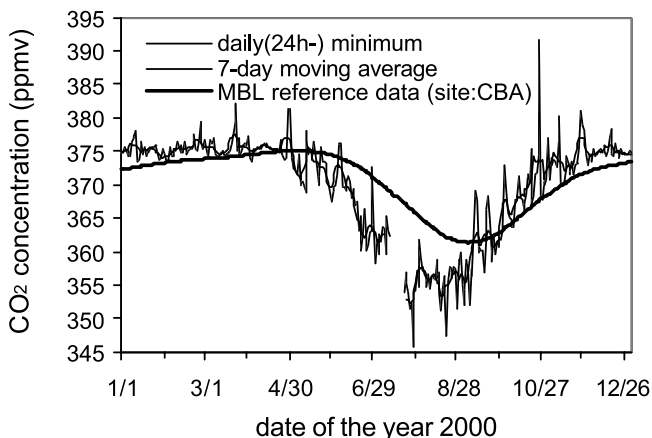


Figure 3. Comparison of daily minimum CO₂ concentrations at 40 m height and 7-day moving averages at Fraserdale, with marine boundary layer (MBL) CO₂ concentration, from NOAA/CMDL data at site of Cold Bay, Alaska (55.20°N, 162.72°W) for year 2000.

height and the top of the surface layer. Term 1 at the right hand side of equation (16) is the storage below height z_s , and term 2 is the eddy flux at z_s level. According to Hollinger [1994] who found from a *Nothofagus* forest that half-hourly changes in CO₂ concentration throughout a vertical profile within the forest were not significantly different from those above the forest (at 36 m height), we use the observed half-hourly change in CO₂ concentration at 20 m as the storage ratio $\partial C/\partial t$ for our estimate of carbon storage in the surface layer. Hence equation (16) can be rewritten as

$$F_{c,s} = F_{c,c} - \frac{\partial C_{obs}}{\partial t} (z_s - h_c), \quad (17)$$

where $F_{c,s}$ and $F_{c,c}$ are the net CO₂ fluxes at the top of the surface layer and at the canopy level, respectively, and $F_{c,c} = NEP$, C_{obs} denote the observed CO₂ concentration at 20 m height.

[26] Because heat energy and carbon share similar vertical variation patterns in storage terms, the sensible heat flux at the top of the surface layer can also be expressed as

$$Q_{h,s} = Q_{h,c} - \rho c_p \frac{\partial \theta_{obs}}{\partial t} (z_s - h_c), \quad (18)$$

where θ_{obs} is the observed potential temperature of air at 20 m height.

2.5.2. Top Boundary Conditions

[27] The sensible heat flux above 2.5 km from the ground ($Q_{h,2.5}$, usually above CBL) is set to zero throughout the year. However, as 1-D model boundary conditions, it is critical to determine the time-dependent CO₂ concentration at the top of CBL ($C_{251/2}$). Unfortunately, large spatial and temporal variations in $1/2$ -atmospheric transport, the CBL development, and the surface CO₂ fluxes make it impractical to directly select regional observations (tower data) or global measurements (e.g., marine boundary layer (MBL) data from flask sampling network) as the top boundary conditions.

[28] Long-term observations at both the North Carolina (NC) tower and Wisconsin (WI) tower showed that strong diurnal variations occur near the surface and rapidly weaken with increasing height [Bakwin *et al.*, 1995, 1998]. Bakwin *et al.* [1998] reported that the difference of CO₂ mixing ratio from near the ground to 400–500 m heights is only 1–3 ppmv during the afternoon but over 40 ppmv during midnight to early morning in summer (see also Figures 10a and 10b). Daily minima and amplitudes of CO₂ concentration at different levels (11–496 m) at both the NC tower and the WI tower were calculated for 1998. The results showed that (1) the daily minima of CO₂ were similar from the ground to 500 m height; and (2) the daily amplitudes of CO₂ decreased with increasing height resulting in little diurnal variation at 400–500 m above the ground. From these observations, the CO₂ concentration around the top of PBL (typically within PBL) may be approximated with the daily minima in the surface layer and exhibit slight diurnal variations. Hence a 24-h minimum value of CO₂ concentration at Fraserdale (49°52′29.9″N, 81°34′12.3″W) 20 m or 40 m height obtained after applying a 7-day moving average could be used to represent the top boundary condition of CBL at all times in a day during the CBL development until the CBL height exceeds that on the previous day.

[29] An alternative approach might be to use nearby marine CO₂ flask measurements as a proxy for the top boundary condition. Background surface stations in the NOAA/CMDL flask-sampling network (GLOBALVIEW-2001) are located to obtain data representing the large spatial scales. Consequently, most stations are remote from strong source or sink regions and measurement protocols stress sampling of air uncontaminated by regional surface processes [Stephens *et al.*, 2000]. However, over the distance from the coast to the continental site, the MBL CO₂ concentration is modified by land, especially at the lower levels. It is therefore incorrect to use MBL CO₂ data as the top CBL condition for all times in a day during the CBL development or for days when the CBL is not fully developed. However, because of the vertical mixing, MBL CO₂ concentration would also have influence on CBL concentration on a daily basis to a small extent. We therefore need to develop a scheme to use the MBL data as part of the top boundary condition.

[30] We have compared 7-day moving averages of 24-hour minimum concentrations at Fraserdale (FRD) 40 m height to the CMDL data from Cold Bay, Alaska (55.20°N, 162.72°W), an upstream marine boundary layer site of a comparable latitude. As Figure 3 shows, wintertime CO₂ in the CBL over the terrestrial region near FRD was slightly higher than that at Cold Bay, as expected due to ecosystem respiration. During summer when the sequestration by ecosystems was active, the CO₂ concentration in the CBL was much lower at FRD than at Cold Bay (Figure 3). Generally, the seasonal cycles of atmospheric CO₂ at continental sites lead those of the MBL since the seasonal cycles over the northern hemisphere are driven primarily by terrestrial ecosystems [Bakwin *et al.*, 1998].

[31] This analysis illustrates that neither the MBL observations in the flask sampling network alone, nor the 24-hour minima tower measurements are sufficient for determining the 1-D model (e.g., the VDS) top boundary condition

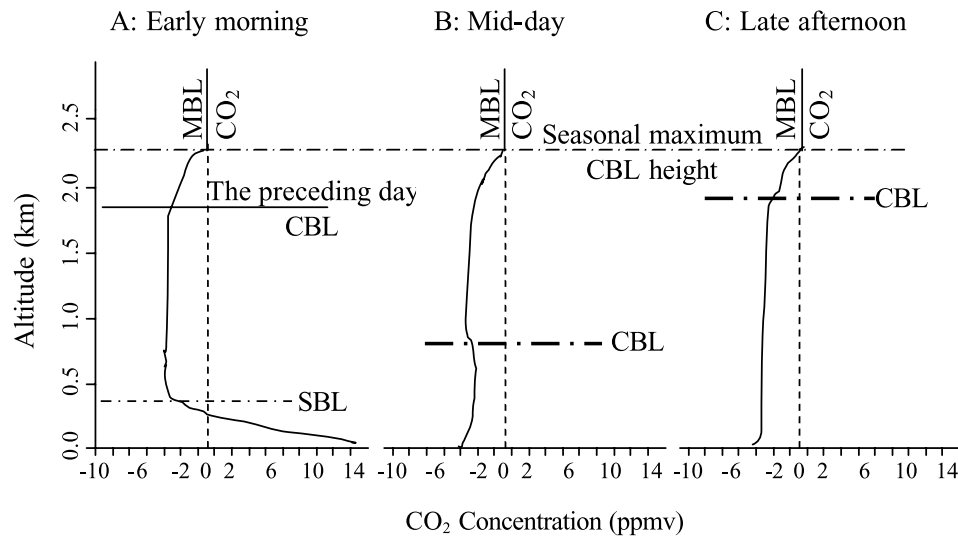


Figure 4. A typical evolution of CO₂ vertical profiles over land during a summer day, resulting from the covariance between PBL (including stable boundary layer (SBL) and convective boundary layer (CBL)) convection and land surface CO₂ flux. The height above which the marine boundary layer (MBL) applies is variable with season and is treated as the monthly maximum CBL. The MBL CO₂ concentration has only a small effect on the lower CO₂ profile during the day. SBL height is predetermined (see Table 1).

because MBL has only very small effects on the mixed layer until it is sufficiently high. The combined use of both may be a solution. Normally, MBL data could represent the atmospheric CO₂ concentration above the seasonal maximum CBL height, above which the surface influence is negligible over one passage from ocean to land. Since CO₂ diffusion is weak in the residual boundary layer [Yi *et al.*, 2001], a transition zone might exist between the seasonal maximum and minimum CBL heights (Figure 4). This transition zone could be approximately set between the seasonal maximum CBL height and the maximum CBL height on a given day. A first-order closure scheme (*K*-theory) is applicable to simulate CO₂ diffusion in this transition zone. The Holtslag boundary layer parameterization [Holtslag and Moeng, 1991; Holtslag and Boville, 1993] is used to parameterize the transport in the transition zone,

$$\frac{\partial C}{\partial t} = \frac{1}{\rho} \frac{\partial}{\partial z} \left[\rho K_c \left(\frac{\partial C}{\partial z} - \gamma_c \right) \right], \quad (19)$$

where γ_c (m⁻¹) is the nonlocal transport term and is neglected in our 1-D model; K_c is the coefficient of vertical diffusivity. K_c is set to decrease linearly with height from the maximum CBL height of a given day (a value of

0.2 m² s⁻¹) to the seasonal maximum CBL height (a fixed value of 0.1 m² s⁻¹), and below the daily maximum CBL height (a fixed value of 0.2 m² s⁻¹). Taking the 7-day moving averages of daily minimum CO₂ as the initial value below the daily maximum CBL height, and selecting the MBL CO₂ data as the top boundary condition at the seasonal maximum CBL height, the CO₂ concentration profile from the sunset to the next morning, at each level within and below the transition zone can be estimated using equation (19). As the time lapses from the sunset, the MBL CO₂ concentration influence gradually increases near the top of the daily maximum CBL. The depth of the daily influence below the daily maximum CBL mainly depends on the difference between MBL CO₂ and the daily minimum CO₂, and on the thickness of the transition zone. The weak mixing in the transition zone modifies slightly the upper air near the top of CBL continuously, while the top boundary condition during CBL development is mostly determined by the profile of the previous day determined by the smoothed daily minimum values.

[32] A typical diurnal evolution of the CO₂ vertical profile over land during summer is schematically illustrated in Figure 4. The photosynthetic uptake is distributed through a thick atmospheric layer associated with the depth of CBL (Figure 4c). The CBL collapses at around sunset,

Table 1. Monthly Maximum and Average Heights of Stable Boundary Layer (SBL) and Convective Boundary Layer (CBL) Over a Boreal Forest Region Near the Fraserdale Tower, Estimated for the Mean Conditions in 1987–1991 (marked with “a”) and Modeled for 2000 Using VDS

PBL, m	Jan	Feb	March	April	May	June	July	Aug	Sept	Oct	Nov	Dec
SBL ^a , mean	417	404	520	404	330	377	272	387	439	462	513	560
CBL ^a , mean	1057	1115	1280	1220	1530	1466	1588	1504	1347	1166	1324	1365
CBL, mean	1038	1112	1297	1315	1486	1587	1483	1402	1284	1168	1076	1093
CBL, max	1568	1692	1783	1951	2126	2341	2102	1939	1928	1848	1638	1460

^aReference data from SENES [1997].

and CO₂ accumulates to high values under the SBL due to nighttime respiration at the surface. The CO₂ concentration above the SBL remains unaffected by the surface at nighttime and only changes slightly from the preceding afternoon to early morning (Figure 4a). Atmospheric CO₂ above and below the preceding day's maximum CBL height mixes slightly as determined by equation (19) (Figure 4a). With these diurnal evolution mechanisms of CO₂ vertical profile over land, we have therefore selected the CO₂ concentration at each level within and below the transition zone computed using equation (19) as the top boundary condition.

[33] As shown in Figure 3, the smoothed curve still contains considerable variations at a 3–10 day time scale corresponding to synoptic scale variations. These synoptic variations may well represent the true top-boundary conditions as low-pressure systems usually come with high CO₂ concentration in the atmospheric column with large vertical extent, and high-pressure systems are associated with low CO₂ values.

2.6. Initialization and Computational Procedures

2.6.1. Initialization

[34] The VDS needs to be initialized at the very beginning (00:00:00) of each season. We initialize potential temperature (θ_j) with the assumption that it changes linearly with height from the lower surface layer to the top of the modeling domain (2520 m) at midnight,

$$\theta_j = \theta_s - (\theta_s - \theta_J) \frac{z_j - z_s}{z_J - z_s}, \quad (20)$$

where subscripts s, J are the values at the top of the lower surface layer and the top of the modeling domain, respectively, and j denotes each cell from $j = 0$ to J . The observed potential temperature (θ_{obs}) of air at 20 m at the very beginning moment (00:00:00) of each season is used for θ_s (when $j = 0$); and its corresponding $\theta_J = \theta_s + \Delta\theta_{s,J}$ (when $j = J$). $\Delta\theta_{s,J}$ equals 6 K for winter, 8 K for spring, 10 K for summer, and 9 K for autumn.

[35] We separately initialize CO₂ concentration (C_j) in the atmosphere below and above the seasonal mean height of the SBL (Table 1). Below the top of SBL, the following equation is used,

$$C_j = C_s - (C_s - C_{SBL,top}) \frac{\ln[z_j/z_s]}{\ln[(z_{SBL,top} - z_s)/z_s]}, \quad (21)$$

where subscripts s and SBL, top , represent the values at the top of the lower surface layer and the top of SBL, respectively; and j denotes each cell from $j = 0$ to $int(z_{SBL,top}/100)$. The observed CO₂ concentration at 20 m at the very beginning moment (00:00:00) of each season is introduced for C_s (when $j = 0$); while the corresponding $C_{SBL,top}$ is set to equal the 7-day moving average of daily minimum CO₂ concentration centered at the beginning of each season. Above the SBL, the CO₂ concentration at each level within and below the transition zone at the beginning (00:00:00) of each season is computed using equation (19) and used as its initial value.

2.6.2. Computation Procedures

[36] The evolution of the CBL for the whole year is simulated first, then the top boundary condition for the CO₂

simulation is computed using equation (19) based on the CBL height (daily and seasonal maximum data), 7-day moving average of the daily minimum CO₂, and the interpolated daily MBL CO₂ concentration. At the second step, the surface scaling parameters are computed, and the bulk Richardson number (R_b) and the stability parameter $|z_h/L|$ are checked to determine the applicable module (see also Figure 1). Then the air potential temperature and CO₂ mixing ratio within/above the lower surface layer are computed from equation (2) in the K -theory module and equations (5) and (15) in the free convection module. A small time step Δt is chosen for maximum accuracy. In the present VDS model, $\Delta t = 60$ s.

3. Results

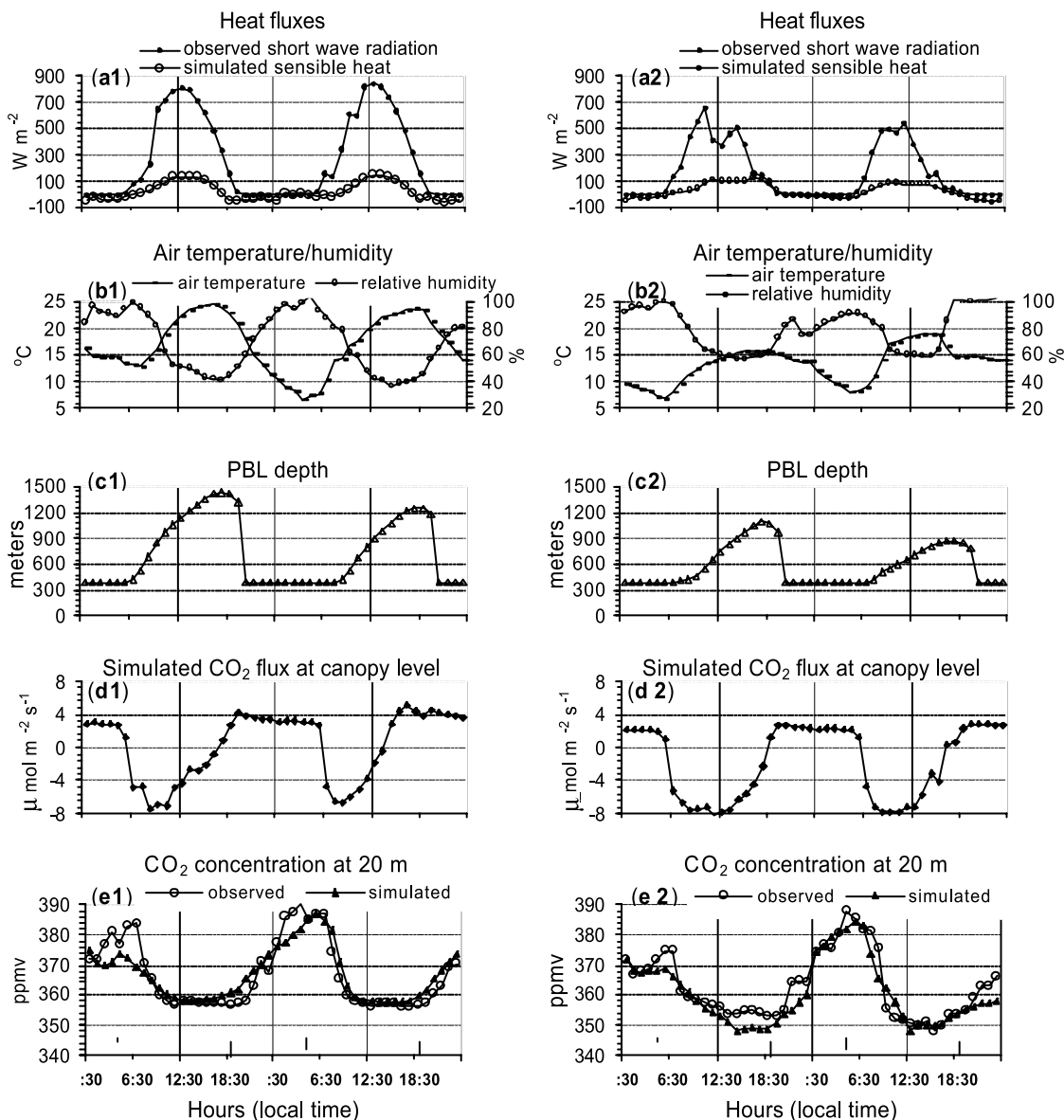
[37] Atmospheric CO₂ concentration and meteorological measurements have been made on a 40 m high tower for the last 10 years at 5-min intervals over a boreal forest site near FRD, Ontario, Canada [Higuchi *et al.*, 2003]. The integrated VDS model was initially run using this tower meteorological data for 11 years (1990–2002, excluding 1997–1998). CO₂ concentration measurements at 20 m and 40 m of this tower were used to validate the model.

3.1. Diurnal Time Series

[38] Observed and simulated diurnal variations of several near-surface/PBL variables for 4 days in the growing season are shown in Figure 5. In order to compare the modeled results under different weather conditions, the results for two clear days (9–10 August 2000) and the same dates in 1999, but under cloudy-shower weather conditions, are shown as a comparison.

3.1.1. Net CO₂ Flux

[39] The net CO₂ flux to the atmosphere simulated by BEPS (Figure 5: d1, d2) was nearly constant at night with a slight decline from sunset to sunrise (from about 4 to 3 $\mu\text{mol m}^{-2} \text{s}^{-1}$), then became negative around sunrise and quickly reached the minimum value of about $-8 \mu\text{mol m}^{-2} \text{s}^{-1}$ by the midmorning (usually around 0930 LT in August). Uptake due to photosynthesis decreased slowly during the afternoon and ceased at about sunset. After sunset the flux became positive again. The net CO₂ flux had similar magnitudes and diurnal patterns for both clear days (2000) and cloudy-shower days (1999) (Figure 5: d1, d2) even though the incoming radiation fluxes were obviously different (on 9–10 August 1999, it only reached 70% of those on the corresponding days in 2000; Figure 5: a1, a2). This reflects the fact that photosynthesis is sensitive to air humidity but respiration is sensitive to air temperature: photosynthesis on the both sunny days in 2000 was constrained by low air humidity (<50% in 2000 versus >60% in 1999) during daytime but respiration was enhanced by high air temperature (24h-mean air temperature: 17.7 and 16.1°C in 2000 versus 12.1 and 13.9°C in 1999) (Figure 5: b1, b2). Different weather conditions also caused dissimilar diurnal NEP patterns (Figure 5: d1, d2). On clear days in 2000, the photosynthesis rate only kept its maximum values for around 2 hours (0930–1030 LT) and then gently declined as air relative humidity decreased, although the incident photosynthetic active radiation (PAR) remained high during these hours (Figure 5: a1, b1, d1). This response was mainly



1: Date, 9th-10th August 2000

2: Date, 9th-10th August 1999

Figure 5. Diurnal time series of near-surface/PBL variables for four days at Fraserdale (49°52'29.9" N, 81°34'12.3" W), Ontario, Canada. 1 (left) for two clear-sunny days; 2 (right) from a cloudy day to a shower day (Kapuskinga data: rain = 2.4 mm d⁻¹, the nearest station (49.42°N, 82.47°W) from Fraserdale). (a) Observed short-wave radiation and simulated sensible heat fluxes by the EASS model in the surface layer. (b) The corresponding measurements of air temperature, humidity at 10 m height. (c) Simulated PBL depth. (d) Simulated CO₂ flux by BEPS (positive for upward fluxes). (e) Simulated and observed CO₂ concentration at 20 m height (the observed hourly data were averages of original six discrete measurements with accuracy of 0.1 ppmv; the range of the six data points within an hour was mostly less than 2 ppmv). Triangles indicate the times of sunrise and sunset.

due to the high sensitivity of stomatal conductance to the air vapor pressure defect (VPD). By contrast, on the corresponding days of 1999, optimal photosynthesis rates maintained over six hours when PAR was high, and then decreased sharply as PAR decreased. On these days, VPD was not a strong limiting factor (Figure 5: a2, b2, d2).

3.1.2. PBL Height

[40] Under clear/sunny weather conditions, the depth of the turbulent CBL (into which CO₂ and heat are “mixed”)

follows a daily cycle with stable nocturnal conditions restricting mixing to about 350 m until around 0930 LT followed by rapid growth during about 1030–1330 LT, reaching a maximum of around 1.25–1.45 km in mid-afternoon (Figure 5: c1). The depth of the CBL only reached a maximum of 0.8 km on 10 August 1999 under cloudy-shower conditions (but on 9 August 1999, it approached 1.05 km) (Figure 5: c2). The simulated maximum sensible heat flux was only 80 W m⁻² on 10 August as compared

with 120 W m^{-2} on 9 August 1999 (Figure 5: a2). The surface cooling in the late afternoon caused the CBL to decline to around 350 m by sunset.

[41] We noted that there was a time lag of about 3–4 hours between the start of active photosynthesis and the start of intensified turbulent mixing when the surface heating was sufficient to interrupt the nocturnal temperature inversion (Figure 5 c1, c2, d1, d2).

3.1.3. CO₂ Concentration

[42] Simulated CO₂ concentration at 20 m above the ground showed a diurnal oscillation with amplitude of 25–35 ppmv during the growing season. The maximum occurred at about sunrise and the minimum in the late afternoon (Figure 5 e1, e2). The agreement with the observed tower data is generally within a few ppmv most of the time, but on occasions the difference can be as large as 10 ppmv, indicating the inability of the 1-D model to simulate episodes caused by horizontal advection.

[43] Both simulated and observed CO₂ concentrations indicate that the CO₂ diurnal cycle near the ground was driven by both the biological exchange and the PBL dynamics. The net CO₂ fluxes and the CO₂ concentration have somewhat similar curve shapes with a steep decline in the morning and a gentle increase in the afternoon (especially on 9–10 August 2000). The build-up of CO₂ in the surface layer usually ceased at about sunrise when photosynthesis began to exceed respiration. Afterward, CO₂ concentration decreased smoothly for the whole morning (Figure 5: d1, e1). These patterns reflect that high relic nocturnal CO₂ concentration in the near canopy layer was consumed quickly by photosynthetic uptake by midmorning and while the “relic” was nearly depleted and the balance mostly approached. Then CO₂ concentration might decrease quickly by midmorning, but the unstable turbulent PBL that commenced at about the same time as surface heating was sufficient to break the stratified nocturnal stable PBL (Figure 5 c1). This could cause the upper part of the broken nocturnal SBL (typically, 50–350 m from ground) with high CO₂ concentrations (the CO₂ concentrations within the nocturnal SBL were much higher than aloft; these vertical patterns and the “CO₂ inversion” will be shown in section 3.2 and see also Figures 8 and 9.) to mix to the surface due to rapid development of turbulent CBL by late morning (1130–1230 LT). As shown in Figure 5, the CO₂ concentration kept a relative steady minimum value for around 4.5 hours during the afternoon (1230/1330–1630/1830 LT, on average) while the downward net CO₂ flux in the surface smoothly increased and the CBL depth rapidly grew to and maintained its relatively constant maximum until late afternoon. This implies that photosynthetic uptake of CO₂ was approximately balanced by turbulent entrainment of air aloft with higher CO₂ concentration. After sunset, the turbulent CBL collapsed when the heat flux from the surface became negative and the surface uptake of CO₂ by forest ceased and soil/plant respirations once again began enriching the surface layer CO₂. The CO₂ concentration near the ground steadily increased from sunset till the next sunrise while the stratified shallow stable SBL developed and the nocturnal temperature inversion strengthened.

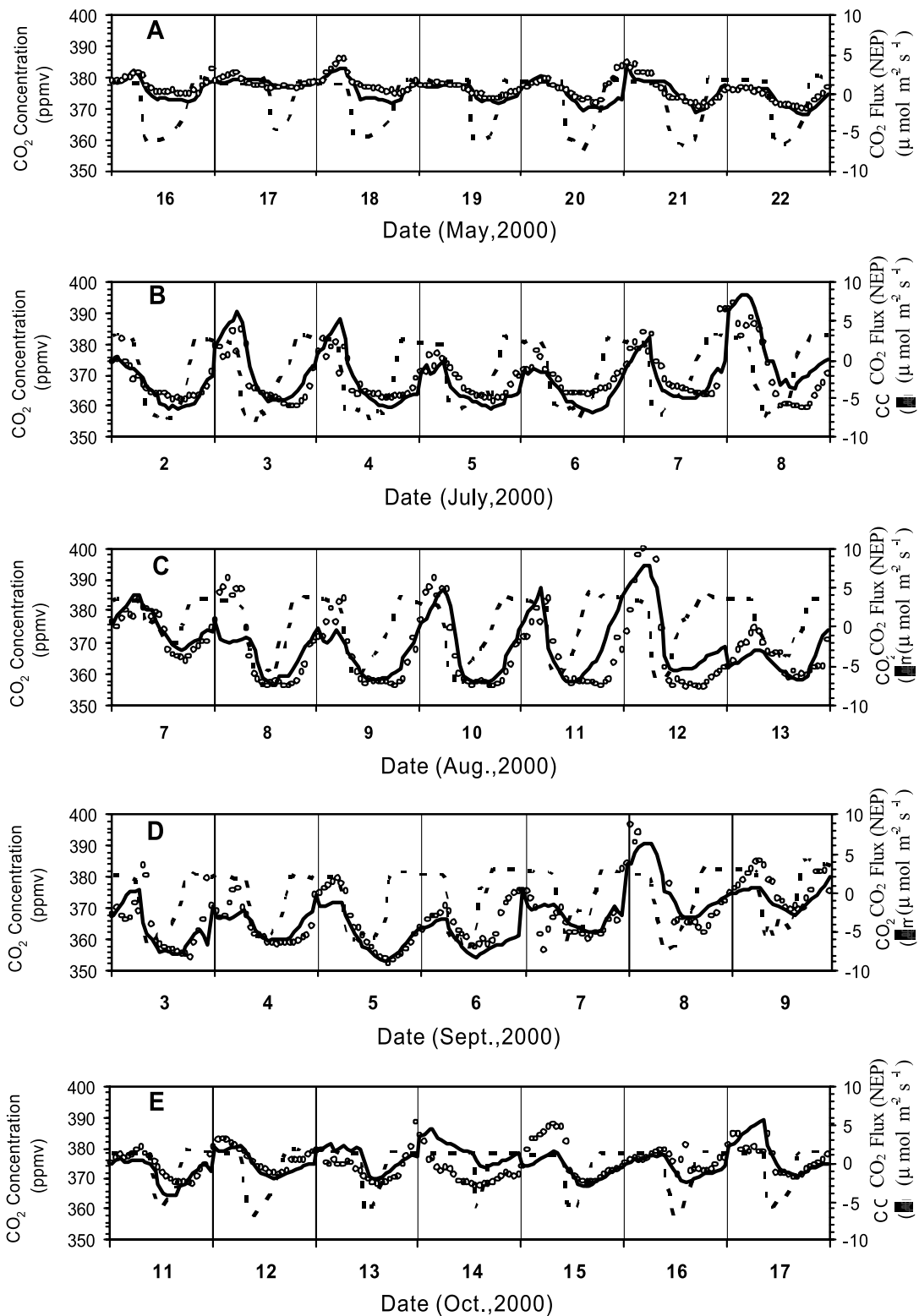
[44] The fact that both the biological sink/source and the PBL dynamics govern variations of atmospheric CO₂ can also be seen from the differences between the two 48 hour

diurnal patterns. Simulated nighttime CO₂ concentrations on 9 August were much lower than that on 10 August, both in 2000 and 1999 (maximum: 374 versus 387 ppmv in 2000 and 369 versus 384 ppmv in 1999) though the source strength for CO₂ provided by respiration was very similar for the two nights (Figure 5: 1d, 2d). The different nighttime CO₂ concentration was mainly controlled by the difference in the nocturnal temperature inversion (the maximum temperature gradients (1.5–40 m high) were $-0.017^\circ\text{C m}^{-1}$ on 9 August versus $-0.175^\circ\text{C m}^{-1}$ on 10 August in 2000 and $-0.05^\circ\text{C m}^{-1}$ on 9 August versus $-0.112^\circ\text{C m}^{-1}$ on 10 August in 1999). The weak inversion during the nights of 9 August (both in 2000 and 1999) formed feebly stable nocturnal condition. This situation led to greater vertical mixing of CO₂ (there was a gradual increase in CO₂ up to 400 m height, see the left part of Figure 8), and consequently the contribution of respiration to the surface layer was diluted by vertical diffusion. In contrast, mixing ratios of CO₂ at the surface layer built up to higher values beneath the stronger nocturnal inversion during the nights of 10 August (both in 2000 and 1999) reflecting the fact that CO₂ diffusion was suppressed under the shallow stable SBL. There was a very small amount of CO₂ diffused above the 200 m height under the stronger nocturnal inversion condition (see the right part of Figure 8).

[45] Contrasting the daytime CO₂ concentration of canopy level flux between the two 48-hour examples further confirms the role of the controlling mechanisms (Figure 5: d1, e1). The temporal structure of the daytime CO₂ concentration for the two days in 2000 is far more similar to each other than the two days in 1999. The contrasting CO₂ concentration for these two days is likely due to different PBL dynamics (1050 m versus 800 m). The fact that the CO₂ concentration declined at a slower rate in the morning and remained at around the lowest values for a longer period on 9 August 1999 than those on 10 August (5 hours versus 1.5 hours) implies that much more of the low CO₂ air aloft was mixed into the surface layer on 9 August than on 10 August.

[46] Simulated 30-min CO₂ concentrations and net CO₂ fluxes during five 1-week periods in 2000 are shown in Figure 6 to illustrate the model performance in different periods of the growing season (early, early-middle, late-middle, late, and last) and under different weather conditions (clear, cloudy, and rainy). The growing season starting in May and ending in October was estimated from daily minimum and average air temperatures (Table 2). The leaf area index (LAI), an important input to BEPS, was a weighted average of 1-km resolution LAI images extending out 30 km around the FRD site [Chen *et al.*, 2002]. Monthly and annual mean NEP values simulated by the BEPS are also listed in Table 2.

[47] In the early growing season (in May, about 2 weeks after the end of dormancy), the photosynthetic rate was small due to low soil temperature, though radiation had risen to above 800 W m^{-2} around noon on fair weather or clear days. Consequently, the diurnal variations of CO₂ concentration were small (Figure 6a). Diurnal variations of CO₂ became more and more noticeable from the beginning of July to the end of August due to the increase in both photosynthesis and PBL depth (Figures 6b and 6c). However, the situation became reversed starting in early



○ Observed CO₂ concentration — Simulated CO₂ concentration ····· NEP by BEPS

Figure 6. Diurnal patterns of half-hourly CO₂ concentrations at 20 m height above the ground in different phases during the growing season in 2000, over a mostly intact boreal forest (*Black spruce*) near Fraserdale, Ontario, Canada. Growing season phases: A, early (about two weeks after the end of dormancy); B, early-middle; C, late-middle; D, late; and E, last (up to the beginning of dormancy). The observed hourly data were averages of original 6 discrete measurements with accuracy of 0.1 ppmv; the range of the six data points within an hour was mostly less than 2 ppmv.

Table 2. Measured Monthly Minimum/Average of Air Temperatures, Precipitation, and Simulated NEP Using BEPS for 2000

Item	Jan	Feb	March	April	May	June	July	Aug	Sept	Oct	Nov	Dec	Annual
Mean Temp, deg C	-18.7	-12.2	-3.3	0.4	9.3	12.1	16.1	14.9	9.9	5.1	-1.9	-18.7	1.42
Min Temp, deg C	-25.2	-19.0	-10.3	-5.3	4.6	6.1	9.9	9.8	5.6	0.5	-3.2	-24.0	-4.33
Precipitation, mm d ⁻¹	1.35	0.41	1.55	0.67	3.82	4.48	3.52	3.62	1.94	1.48	1.32	1.51	2.15
NEP, gC m ⁻² d ⁻¹	-0.38	-0.09	0.20	0.56	2.83	2.07	0.69	-0.40	0.37	-0.02	-0.78	-0.46	0.38

September because both radiation and temperatures began to decrease substantially. The 24-hour amplitude of CO₂ oscillation decreased quickly to the level of the early growing season by the middle of October when the growth dormancy began (Figures 6d and 6e). Regression analysis (Figure 7) of the 30-min CO₂ concentration using data from the five 1-week periods presented above ($n = 840$) gives a linear correlation coefficient (R) of 0.81. The model generated the overall changing patterns of the observed values at the tower, both in amplitude and phase, under different weather conditions. However, noticeable mismatches still occurred in some cases (e.g., 8 and 13 August and 14–15 October) (Figure 6), particularly in the late growing season (the linear correlation coefficient in October only reaches 0.5) (Figure 7). The presented VDS model only considers the vertical diffusion processes in the surface and mixed layers. Thus such a model could be in error under advection conditions associated with synoptic weather systems.

3.2. Simulated Vertical Diurnal Profiles

[48] The amplitude and phase of the diurnal cycle of simulated CO₂ concentration during the growing season agree closely with the observations at the surface layer, giving us confidence in the simulated vertical profiles in the CBL. The simulated vertical diurnal profiles are different under different weather conditions.

[49] Under sunny conditions in daytime in summer, there was net CO₂ uptake at the surface (photosynthesis greater than respiration) while air aloft with higher CO₂ concentration was entrained by the well-mixed convective PBL, typically 1–2 km in height (Figure 5: c1). Therefore CO₂ concentrations during the daytime in the growing season were lower than the 24-hour mean values through the whole vertical model domain. CO₂ concentrations decreased from the early morning to the mid-day and the minima occurred during the afternoon while the mixed layer grew to about 0.8–1.5 km (Figure 8). A 1–3 ppmv decrease in CO₂ concentration from the top of PBL to the surface layer was also modeled (Figure 8). The results are similar to the WI and NC high tower observations with 1–3 ppmv variations with height in the lower part of the CBL [Bakwin *et al.*, 1998; Denning *et al.*, 1996b] (see Figures 10a and 10b). By contrast, vertical CO₂ diffusion was weak under cloudy-rainy conditions when the convective PBL was shallow and feeble. Consequently, the time-height field showed a gradual increase in CO₂ concentration with increasing height during the daytime (Figures 9a and 9b). Moreover, the times of maximum and minimum concentration occurred about 5–6 hours later at 1 km height than in the surface layer (Figure 9b).

[50] After sunset, the convective PBL weakened and disappeared quickly, and the CO₂ concentration once again began to increase due to soil respiration. As discussed

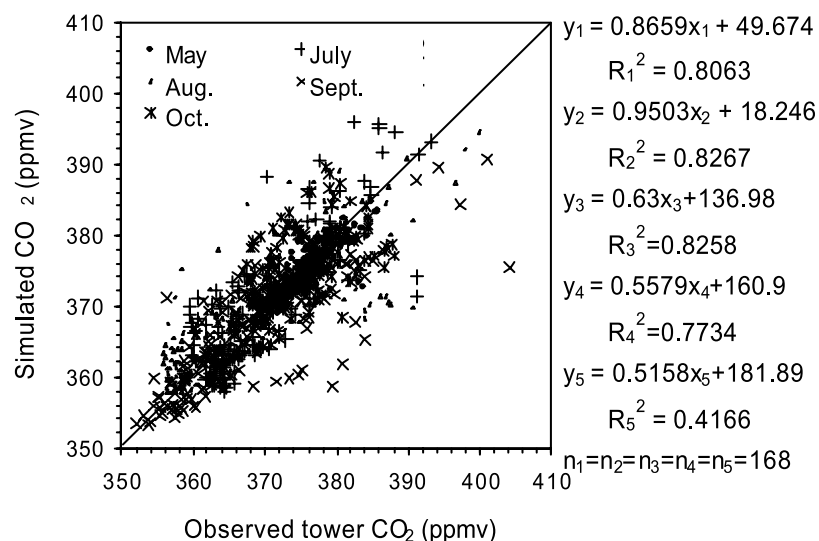


Figure 7. Linear regression relationship between simulated and measured half-hourly CO₂ concentrations at 20 m height during the growing season in 2000 at Fraserdale, Ontario, Canada. Here y and x represent simulated and observed CO₂ concentrations, respectively; R and n denote the linear correlation coefficient and sample number, respectively; subscripts 1–5 denotes the group of samples shown in Figure 9 (A to E: May to Oct.).

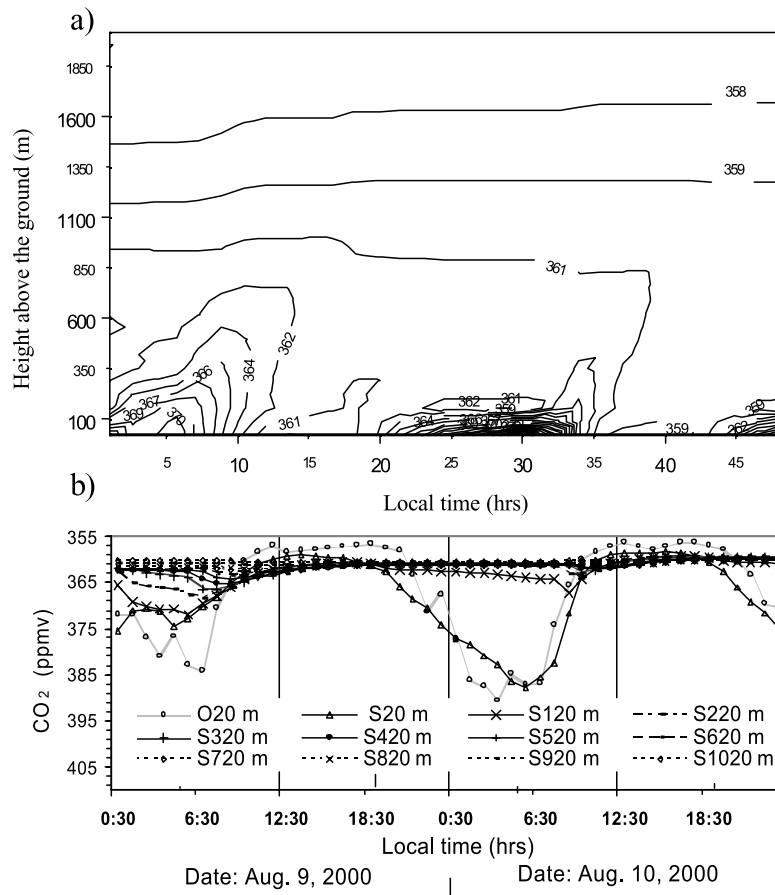


Figure 8. Time-height cross section of simulated (multiple heights) and observed (20 m) diurnal variations of CO₂ concentrations for two days (under clear-sunny weather conditions; 9–10 August 2000). (a) 2-D CO₂ concentration contour graph (unit: ppmv); (b) vertical profile of diurnal cycles of CO₂ (up to 1020 m, O is tower observed, S is simulated). Triangles indicate the times of sunrise and sunset.

above, the very strong nocturnal temperature inversion under clear conditions suppressed CO₂ diffusion in the shallow stable PBL. In contrast, residual daytime air with low CO₂ was present above the PBL. This led to a very strong nocturnal “CO₂ inversion” as described by Denning *et al.* [1996b], characterized by a gradient in CO₂ concentration of about 25–30 ppmv across the PBL top by the next sunrise (Figure 8 for 9 August night to 10 August morning). This is similar to the simulated result using a 3-D circulation model [Denning *et al.*, 1996b]. The strength of the “CO₂ inversion” was positively related to the strength of the nocturnal temperature inversion. This is indicated by comparisons shown in Figure 5. The weaker the temperature inversion, the greater the height to which CO₂ transport occurs. For example, it was rainy on 8 August 2000, and there was a weak temperature inversion during the following night. Correspondingly, the release of CO₂ from soil respiration could diffuse to 400 m (Figure 8) and only 12 ppmv of the “CO₂ inversion” was formed. However, over 30 ppmv of the “CO₂ inversion” occurred the next night (Figure 8) under a strong temperature inversion.

[51] Simulated vertical diurnal profiles of CO₂ concentration under different weather conditions in the growing season (Figures 8 and 9) are similar in patterns to the results presented by Denning *et al.* [1996b] using the Colorado

State University (CSU) General Circulation Model (GCM) and are also consistent with the high tower observations (Figures 10a and 10b) [Bakwin *et al.*, 1998]. Figure 10 summarizes the simulated diurnal cycles over a boreal forest region near FRD, compared with measurements at the NC and WI towers. Both simulations and observations show similar vertical patterns (Figures 10a, 10b, and 10c). Strong diurnal variations occurred near the surface layer, and the magnitudes of the diurnal cycle were damped and had a time lag with increasing height. The modeled results (Figures 8 and 9) illustrate again that the CO₂ diurnal vertical diffusion process was modulated by diurnal variations of ecosystem carbon sink/source, diurnal PBL dynamics, and the strength of the atmospheric nocturnal temperature inversion. However, the simulated CO₂ diurnal cycles at around the seasonal mean PBL height (e.g., 1483 m for July 2000) (Table 1) were very weak, and the CO₂ concentrations at those levels were about 3–4 ppmv higher than at the near ground in the afternoon during the growing season (e.g., July 2000) (Figure 10c). This implies that the CO₂ mixing ratios in the upper part of the vertical profile (around the seasonal mean PBL height) are dominated by the background CO₂ in the troposphere. These simulated results demonstrate the ability of VDS to follow the vertical transfer processes overall.

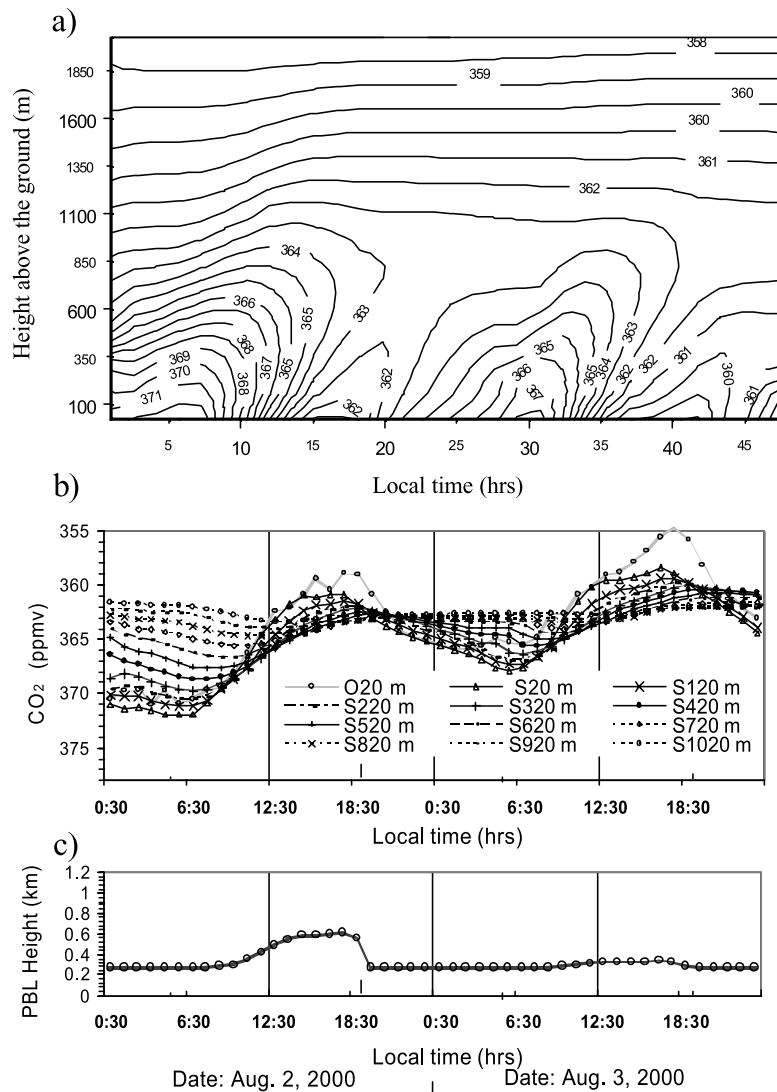


Figure 9. Time-height cross section of simulated (multiple heights) and observed (20 m) diurnal variations of CO₂ concentrations (under cloudy-rainy weather conditions; 2–3 August 2000). (a) CO₂ concentration contours (unit: ppmv); (b) Vertical profiles of diurnal cycles of CO₂ (up to 1020 m, O is tower observed, S is simulated); (c) height of the convective PBL. Triangles indicate the times of sunrise and sunset.

[52] The monthly mean diurnal amplitudes at different heights over the boreal region surrounding the FRD tower are shown in Figure 10d. Their maxima were found in July–August while the minima were found in January–December at all heights. Furthermore, the mean amplitudes were greatest near the surface and rapidly decreased with increasing height. The largest vertical difference in amplitude occurred during the July–August period and was over 20 ppmv. The smallest difference was only 2–7 ppmv and occurred during November to March. The monthly composite diurnal amplitudes decreased logarithmically with increasing height and were different from month to month (Figure 10d). This decline was more pronounced during the growing season, as a consequence of the large magnitudes of both photosynthesis and respiration during the growing season.

3.3. Seasonal Cycle

[53] Figure 11 shows simulated (and observed at 20 m height) monthly averages of CO₂ mixing ratios at different

heights from 20 m to 2520 m above the ground, illustrating the seasonal cycles over the boreal region surrounding the FRD tower. The simulated peak seasonal values (375–377 ppmv) at each height occurred in March, followed by a gradual decrease to May, then by a rapid decrease down to annual minima during the growing season (Figure 11). The simulated minimum CO₂ values occurred in August below the annual mean CBL height (with exception of at the lower surface layer (20 m), see Figure 11a), while in September, the minimum occurred above the annual mean CBL height (Figure 11b). A rapid increase occurred through the fall at each level, reflecting a decrease in photosynthetic uptake during the fall. CO₂ concentrations in the whole model domain gradually increased from November to March in the following year (Figure 11) due to the dominance of soil respiration. This suggests that CO₂ concentrations increase in fall and in winter due to respiration and decrease in summer due to photosynthetic uptake.

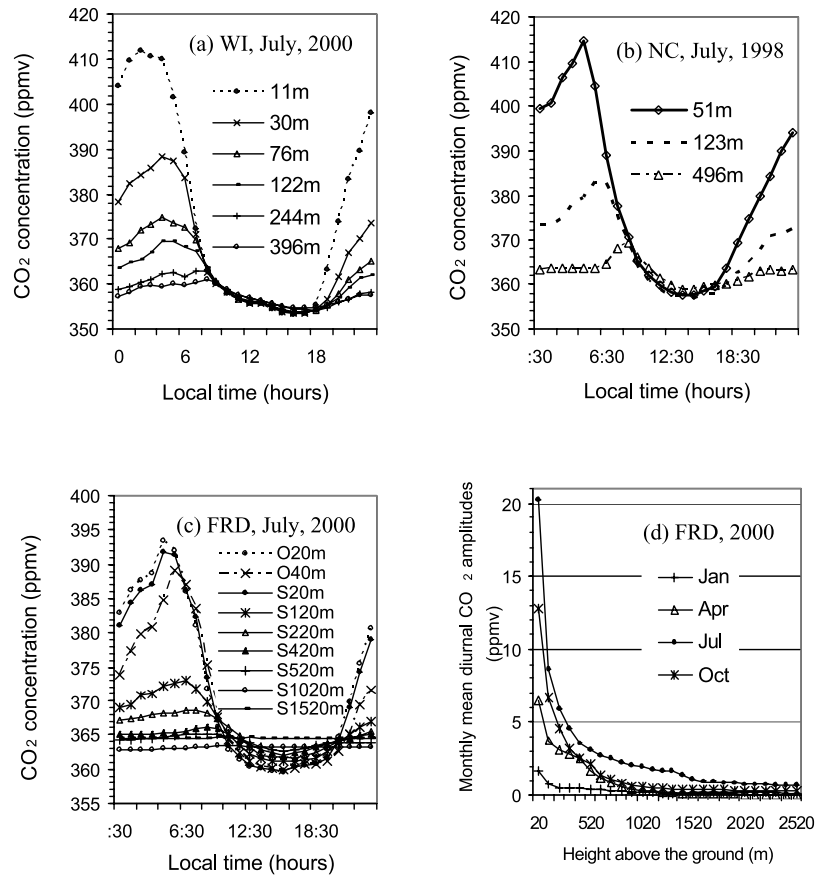


Figure 10. Comparison of simulated and observed monthly composite diurnal cycles of CO₂ concentration (medians by hour) in the PBL. (a) Measurements for July of 2000 on the Wisconsin (WI) tower. (b) Measurements for July of 1998 on the North Carolina (NC) tower. (c) Simulations for July of 2000 over a boreal region near Fraserdale, Canada (FRD). (d) Vertical profiles of monthly mean diurnal amplitudes from the ground to 2.5 km for the year 2000 at the FRD site.

[54] The vertical pattern of CO₂ seasonality within the annual mean CBL was different from that above the CBL height (compare Figure 11a with Figure 11b). Within the annual mean CBL, the modeled amplitudes of seasonal

cycles increased with height (from 9.5 ppmv at lower surface up to 16.3 ppmv at the top of annual mean CBL) (Figures 11a and 12). This vertical spatial pattern is comparable to the observations at the NC and WI high towers (Figure 12).

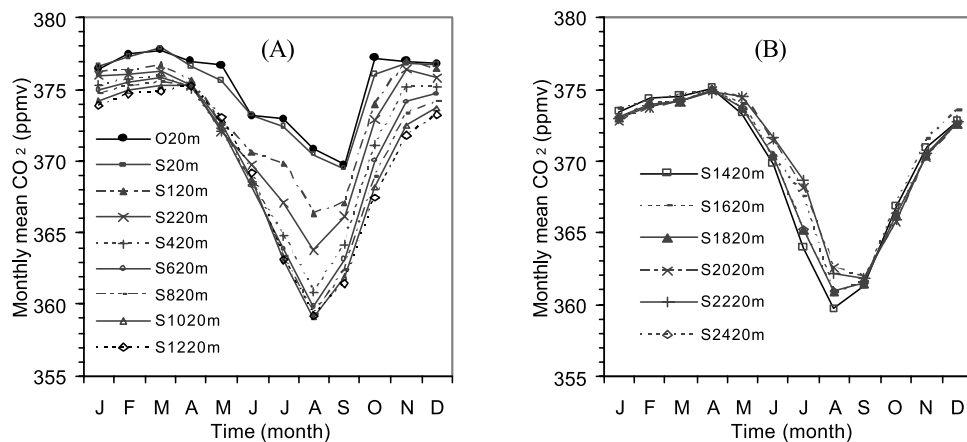


Figure 11. Observed (at 20 m height, O20 m) and simulated monthly mean CO₂ concentrations at different heights (S20 ~ S2420 m) above the ground for the year 2000 over a boreal region near Fraserdale, Ontario, Canada. (a) From the ground up to 1220 m, the seasonal cycle amplitudes increase with height. (b) From 1420 m through 2420 m, the seasonal cycle amplitudes decrease with height and the phase of seasonal cycle shifts with height.

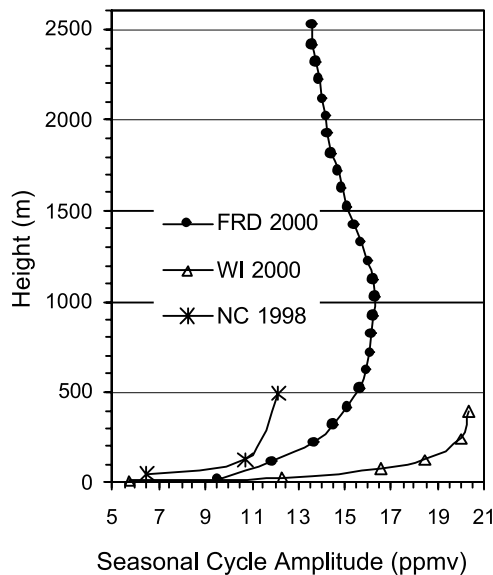


Figure 12. Seasonal amplitudes of CO₂ at each simulated level at FRD site (the year 2000) and at each measurement level on the Wisconsin (WI) (the year 2000) and North Carolina (NC) (the year 1998) towers.

Bakwin et al. [1995, 1998] reported very little seasonal cycle near the ground (7–9 ppmv), but the seasonal amplitudes of 16.9 ppmv at 496 m for 1993–1997 and 22.4 ppmv at 396 m for 1995–1997 on the NC and WI towers, respectively. These vertical patterns were also simulated by a global 3-D circulation model [Denning *et al.*, 1996b]. A clear explanation for this vertical pattern within the annual mean CBL height has been made by Denning *et al.* [1996b] and by Bakwin *et al.* [1998]: the positive seasonal covariance between dynamics of the PBL and carbon flux. Both photosynthetic carbon uptake and ecosystem respiration had large magnitudes during the growing season.

[55] Above the top of the annual mean CBL, the seasonal amplitude decreased with height, from 16.3 ppmv to the atmospheric background value (e.g., MBL data, around 13.5 ppmv) at the top of the model domain (Figures 11b and 12). Moreover, there was a 10–30 day phase delay in the seasonal variation from within the height of annual mean seasonal maximum CBL to the top of model domain (Figure 11b). This suggests the transition zone around the top of seasonal maximum CBL is characterized by both the local ecosystem behavior and the background CO₂ concentration in the free troposphere.

3.4. Atmospheric Rectifier Effect

[56] Similar to the seasonal amplitude, the pattern in annual mean CO₂ concentration below the annual mean seasonal maximum CBL height (around 1.4–1.5 km above the ground) was different from that above (Figure 13). Modeled annual mean CO₂ concentration decreased with increasing height from about 372.99 ppmv at the lower surface layer (20 m) to 369.68 ppmv at roughly 1.5 km, with greater gradients in the lower layers and smaller gradients in the upper layer. However, the simulated annual mean CO₂ concentration gradually increased with increasing height above the annual mean maximum CBL height, as a result of the influence of MBL air from the top (Figure 13).

[57] This vertical pattern below the annual mean maximum CBL height in annual mean CO₂ concentration, agrees with the NC and WI towers observations (Figure 13; also documented by Bakwin *et al.* [1998]). A similar vertical pattern in annual mean CO₂ concentration was also simulated by a 3-D circulation model [Denning *et al.*, 1996b]. However, the vertical gradients were different at different locations: 3.56 ppmv presented here using BEPS-VDS from the ground to 1.5 km height around the FRD tower (49°52′29.9″ N, 81°34′12.3″ W), about 3 ppmv by Denning *et al.* [1996b] from the land surface to 2 km at 60°N, but around 10 ppmv between 51 m and 496 m at the NC tower (35.37°N, 77.39°W, Figure 13) and about 8 ppmv from 11 m to 396 m at the WI tower (45.95°N, 90.27°W, Figure 13). The covariance of the surface net CO₂ flux and vertical transport (mainly by buoyancy convection in the CBL) may be the reason for the annual mean vertical distribution [Denning *et al.*, 1996b; Bakwin *et al.*, 1998; Gurney, 2002]. The annual mean net CO₂ flux at canopy level at FRD site was only 0.38 g C m⁻² d⁻¹ (downward, positive) for 2000 (Table 2), which is much lower than that in the middle-latitude forest region (e.g., 2 ~ 3 g C m⁻² d⁻¹ in the NC and WI towers (cited from the Ameriflux data)). The difference in the cases mentioned above perhaps result from differences in the biospheric uptake and CBL depth at different latitudes (stronger carbon metabolism occurs at lower latitudes in the temperate region, but weaker in the boreal region). The annual mean vertical gradient of CO₂ in the atmosphere, as a quantitative indicator of the atmospheric rectifier effect, is caused by the covariance between the surface CO₂ flux and vertical convection which coherently acted on the same diurnal, synoptic, and seasonal frequencies [Denning *et al.*, 1995, 1996b]. As mentioned above, the simulated atmospheric rectifier effect in the boreal region (e.g., FRD, the study site) was lower than that in the temperate region (e.g., the NC tower measure-

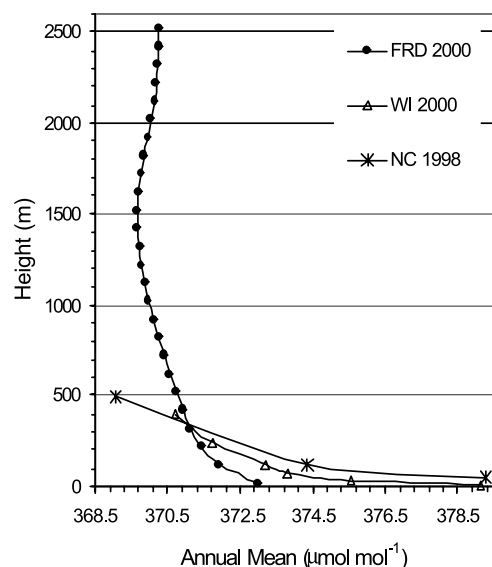


Figure 13. Comparison of vertical profiles of annual mean CO₂ concentration between simulated over a boreal region near FRD for the year 2000 and observed on the WI tower for the year 2000 and on the NC tower for the year 1998.

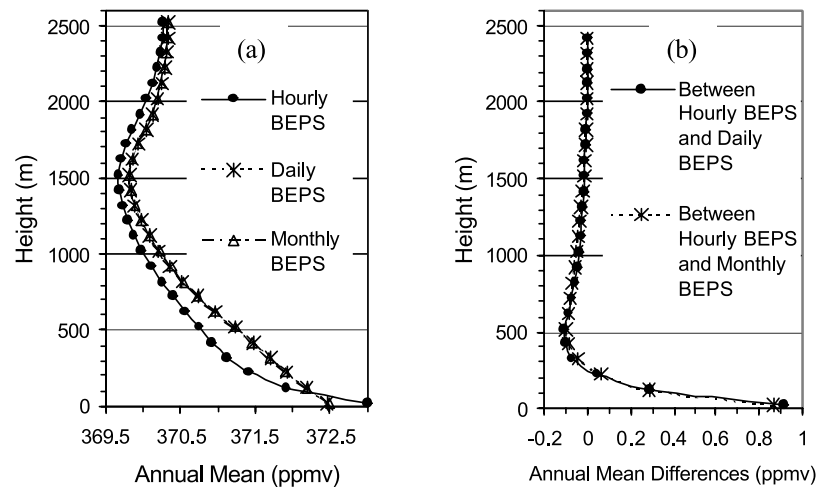


Figure 14. (a) Comparison of vertical patterns in annual mean CO₂ concentration simulated using BEPS at hourly, daily and monthly time steps from the ground to 2.5 km for the year 2000. Daily and monthly calculations are almost identical. (b) The effect of the diurnal cycle on the simulated CO₂ concentration is seen as the difference between hourly and daily/monthly calculations.

ments, Bakwin *et al.*, 1998), but was stronger than that in higher latitudes (e.g., 60°N) [Denning *et al.*, 1996b].

[58] To investigate the contribution of the diurnally varying net carbon flux to the rectifier effect, we performed model sensitivity analysis. We used the daily and monthly mean net CO₂ fluxes calculated from BEPS, respectively, as lower boundary condition to drive VDS (which we refer to as the “daily BEPS” and “monthly BEPS” experiments, respectively). The results were compared to those obtained from model runs using hourly net carbon flux (referred to as the “hourly BEPS”). Simulations using the “daily BEPS” and the “monthly BEPS” resulted in nearly identical annual mean CO₂ concentration profiles (Figure 14a). The annual mean vertical gradient of CO₂ mixing ratio simulated with the “hourly BEPS” was only slightly stronger than that simulated with the “daily BEPS” and the “monthly BEPS” (Figure 14a). These simulated differences, which may be identified as the diurnal rectifying effect, are only 0.92 and 0.88 ppmv and are 25.9% and 24.6% of the total rectifier effect, respectively. Evidently, it is the seasonal covariance between the net CO₂ flux at canopy level and vertical convection that accounts for most of the annual rectifier effect. Furthermore, the model sensitivity experiment shows that the diurnal rectifying effect is confined to shallow layer near the ground (less than 300 m) (Figure 14b). These results are consistent with a simulated result by Denning *et al.* [1996b] that the coupled diurnal rectifier enhances the seasonal effect by about 20% over the northern middle latitudes.

[59] Vertical distributions of the monthly mean CO₂ mixing ratio for the year 2000 are shown in Figure 15. There were large vertical gradients during the growing season with a maximum in August (over 10 ppmv) (Figure 15), while only 1–2 ppmv vertical differences during the nongrowing season (November to April) (Figure 15). This perhaps reflects the seasonal difference in the diurnal rectifier effect. The diurnal rectifier effect is much more pronounced in the growing season when both the photosynthetic uptake during daytime and respiration

release of CO₂ during nighttime are stronger than that in the nongrowing season.

4. Summary and Conclusions

[60] Many aspects of the temporal and vertical spatial variations of atmospheric CO₂ have been simulated in a coupled model that includes the calculation of both the CO₂ and sensible heat fluxes at the surface and the CO₂ vertical transport. The use of a short time step and a selection of different schemes to treat the stable/nocturnal and the free-convection PBL structures provide a high degree of realism. The simulated CO₂ concentration at the surface layer during the growing season agreed well with the observations made at the Fraserdale (FRD) tower, and their linear correlation coefficient (R) reaches 0.81 ($n = 840$). The vertical structure of the simulated diurnal variations of CO₂ in the PBL resembles those observed at the North Carolina (NC) and Wisconsin (WI) high towers. The model simulation illustrates that the CO₂ diurnal vertical diffusion process is modulated by diurnal variations of ecosystem carbon sink/source, diurnal PBL dynamics, and the strength of the atmospheric nocturnal temperature inversion. The amplitude and phase of the seasonal cycle of simulated concentration at the surface layer show good agreement with the FRD tower data. Vertical attenuation of the CO₂ seasonal amplitude within the simulated PBL is comparable to the NC and WI measurements. The simulated annual mean vertical gradient of CO₂ in the planetary boundary layer, in terms of the rectifier effect, in the boreal region (e.g., 3.56 ppmv at FRD, the study site) was lower than that in the temperate region (e.g., 8–10 ppmv at the NC and WI towers observations), but was larger than that in higher latitudes (e.g., about 3 ppmv at 60°N) [Denning *et al.*, 1996b], resulting from the different strengths in the covariance between ecosystem metabolism and vertical diffusion at different latitudes. The seasonal variations accounted for about 75% of the total rectifier effect while the rest was caused by the diurnal variations. The diurnal rectifier effect was mostly

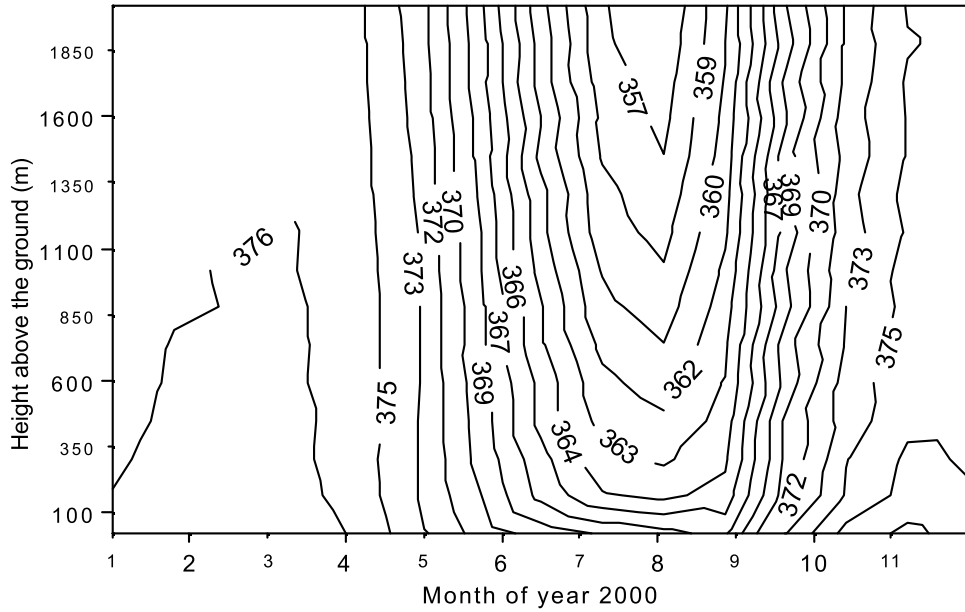


Figure 15. Time-height cross section (up to 2 km) of monthly mean CO₂ concentrations (contour graph); unit: ppmv.

confined to lower heights of less than 300 m. The vertical gradient of simulated monthly mean concentration varied greatly from month to month, suggesting that the diurnal rectifier effect has a strong seasonal variation.

[61] We realize limitations of this 1-D model. The modeled temporal and vertical spatial variations of CO₂ concentration, as well as the simulated rectifier effect, only include the covariance in processes in the vertical direction. Covariance in horizontal transport processes may also be important. This VDS should also serve another purpose (though not shown here): to interpret CO₂ concentration records measured on towers as affected by the ecosystem photosynthesis and respiration in the upwind area.

Appendix A: Algorithm of the Depth of Convective Boundary Layer

[62] The aim of the convective boundary layer (CBL) submodel is to simulate the structure and evolution of the CBL with emphasis on the depth of CBL. The top of the convective mixed layer, z_h , is often defined as the level of most negative heat flux. This level is near the middle of the entrainment zone, often at the height where the capping inversion is strongest (Figure A1) [Stull, 1993]. The equations used in the model are

$$\frac{dz_h}{dt} \Delta\theta = -(\overline{\theta'w'})_{z_h}, \quad (\text{A1})$$

$$\frac{d\Delta\theta}{dt} = \gamma \frac{dz_h}{dt} - \frac{\partial \bar{\theta}_m}{\partial t}, \quad (\text{A2})$$

$$\frac{\partial \bar{\theta}_m}{\partial t} = -\frac{(\overline{\theta'w'})_{z_h} - (\overline{\theta'w'})_0}{z_h}. \quad (\text{A3})$$

In equations (A1–A3), $\Delta\theta$ is the jump in potential temperature θ across the entrainment zone (see Figure A1); γ is the local $\partial\theta/\partial z$ just above the top of the CBL; $\bar{\theta}_m$ is the potential temperature vertically averaged over the CBL depth. Generally, the ratio of $(\overline{\theta'w'})_{z_h}$ to $(\overline{\theta'w'})_0$ is often assumed to be a constant (c) in order to close equations (A1–A3):

$$(\overline{\theta'w'})_{z_h} = -c(\overline{\theta'w'})_0, \quad (\text{A4})$$

where constant $c = 0.1 \sim 0.5$ in literatures and is often given the value of 0.2.

[63] Actually, the ratio of $(\overline{\theta'w'})_{z_h}$ to $(\overline{\theta'w'})_0$ is not a constant, but has a diurnal variation. Hence, here in this

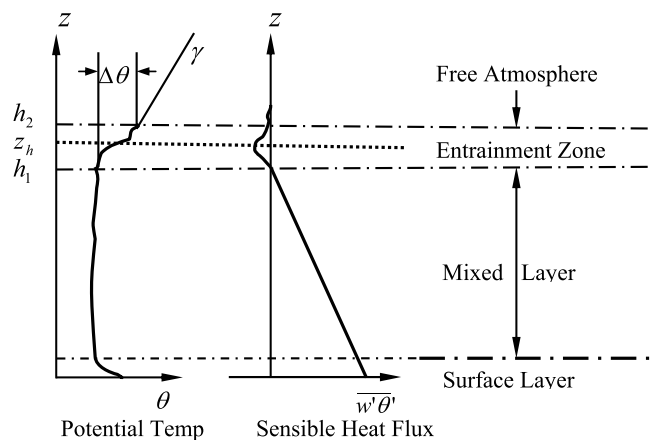


Figure A1. Physical structure of convective boundary layer (CBL) (symbols are defined in the text).

paper, following Zeman [1977], the ratio c is calculated at every time step from

$$c = \frac{C_F - C\omega_B z_h / w_*}{1 + C_T w_*^2 T_s / g z_h \Delta\theta}, \quad (\text{A5})$$

where C_F , C , and C_T are constants, and are set to 0.5, 3.55, and 0.024, respectively, after Zeman [1977], and T_s is the temperature in K at the top of the surface layer.

[64] In equation (A5), the Brunt-Vaisala frequency ω_B in s^{-1} and the free-convection scaling velocity in m s^{-1} are calculated from the following equations, respectively,

$$\omega_B = \left(\frac{g\gamma}{T_s}\right)^{\frac{1}{2}}, \quad (\text{A6})$$

$$w_* = \frac{g z_h}{\theta} \left(\overline{\theta'w'}\right)_0 \quad \text{when} \quad \left(\overline{\theta'w'}\right)_0 \geq 0. \quad (\text{A7})$$

Replacing $\left(\overline{\theta'w'}\right)_0$ in equation (A3) with $\left(\overline{\theta'w'}\right)_{z_h}$ in equation (A4), and then substituting equation (A3) in equation (A1), we obtain,

$$\frac{1}{z_h} \frac{dz_h}{dt} = \frac{c}{(1+c)\Delta\theta} \frac{\partial \bar{\theta}_m}{\partial t}. \quad (\text{A8})$$

Following Garrett [1981], we assume that the changes in $\Delta\theta$ and c within time step Δt are negligible. Substituting equation (A2) with equation (A8) and integrating equation (A8) with respect to time t yields:

$$z_h(i+1) = z_h(i) \exp\left[c(\bar{\theta}_m(i+1) - \bar{\theta}_m(i))(1+c)^{-1}(\Delta\theta(i))^{-1}\right], \quad (\text{A9})$$

where i denotes the time step, $\bar{\theta}_m$ is the potential temperature vertically averaged over the CBL depth, $\Delta\theta$ is the change in potential temperature across the entrainment zone (see Figure A1), and c is the ratio of $\left(\overline{\theta'w'}\right)_{z_h}$ to $\left(\overline{\theta'w'}\right)_0$. $\bar{\theta}_m$, $\Delta\theta$ and c are calculated using equations (A2–A5), while the heat flux at the canopy level $\left(\overline{\theta'w'}\right)_0$ is computed from the EASS model ($\left(\overline{\theta'w'}\right)_0 = Q_{h,s} (\rho c_p)^{-1}$) at every time step. The simulated CBL depth is summarized in Table 1. Monthly average and maximum CBL heights (1587 m and 2341 m) were largest in June and lowest in January (1038 m and 1568 m), with a seasonal amplitude of around 600 m.

Appendix B: Parameterization of Eddy-Transfer Coefficient K

[65] The eddy-transfer coefficient K in different situations is calculated differently as follows:

[66] 1. For case $R_b \geq 0.2$, the surface layer is assumed to be so stable that only very weak turbulence exists; all K -coefficients are set to a low value, equal to 2×10^3 times of molecular thermal diffusivity ν_0 ($= 2.06 \times 10^{-5} \text{ m}^2 \text{ s}^{-1}$); that is $K_c = K_M = K_h = 2 \times 10^3 \times \nu_0 = 4.12 \times 10^{-2} \text{ m}^2 \text{ s}^{-1}$, where subscripts c , M , and h denote gradient-transfer coefficients for CO₂, momentum, and heat, respectively. In our study, we use approximately

the same values though different variables are associated with different K values as discussed below.

[67] 2. When $R_b < 0.2$, the K value depends on the atmospheric stability. We use Blackadar's equation to calculate the K -coefficient, which was derived from the second-order closure theory [Blackadar, 1976],

$$K_c = K_0 + \frac{\partial u}{\partial z} (kl)^2 (R_c - R_i) / R_c, \quad (\text{B1})$$

where K_0 is a background value, k is the Von Karman constant; R_c is the critical Richardson number, l is a length that is presumed to characterize the turbulence containing energy, and R_i is the gradient Richardson number. Fixed values of 0.5, 0.25, 100 are used for K_0 , R_c , and l , respectively.

[68] Because wind velocity in PBL is not used in the present model, we adopt the well-known Monin-Obukhov similarity theory to estimate the vertical wind shear term, $\partial u / \partial z$ (vertical gradient) from the ratio $\zeta = z/L$, specifically,

$$\frac{\partial u}{\partial z} = \frac{u_*}{kz} \phi_m(\zeta) \quad (\text{B2})$$

where the friction wind speed at neutral status ($u_* = k u_s / \ln((z_s - d)/z_0)$), where k is the von Karman constant and is set to 0.4, d is a displacement height, and z_0 represents a roughness length), and the dimensionless wind shear in the surface layer (ϕ_m) is calculated using equation 9.7.5 from Stull [1993].

[69] The gradient Richardson number R_i in equation (B1) is calculated from equation (B3) derived by Pandolfo [1966] and modified by Businger *et al.* [1971],

$$Ri = \begin{cases} = 0.74\zeta(1 - 15\zeta)^{\frac{1}{2}} (1 - 9\zeta)^{-\frac{1}{2}} & \text{for unstable } (\zeta < 0) \\ = (0.74\zeta + 4.7\zeta^2) (1 + 4.7\zeta)^{-2} & \text{for stable } (\zeta > 0) \end{cases}. \quad (\text{B3})$$

When the condition $Ri > R_c$ occurs, the relatively strong temperature stratification suppresses the shear-generated turbulence so that the value of K_c is set to K_0 [Zhang and Anthes, 1982].

[70] **Acknowledgments.** We would like to acknowledge Doug Worthy for his measurements of the CO₂ concentration and meteorology data at Fraserdale. We thank Peter Bakwin of the NOAA/CMDL Carbon Cycle Group, who provided the CO₂ concentration data for the North Carolina television tower and Wisconsin tower by GLOBALVIEW-CO₂, 2001. We also thank Pieter Tans of NOAA/CMDL and Scott Denning of the University of Colorado for useful discussions on early part of our results. We also thank the two reviewers who made extensive comments/suggestions which are very helpful to the paper revision. This research is funded by Canadian Foundation for Climate and Atmospheric Sciences.

References

- Baker, D. (2000), Sources and sinks of atmospheric CO₂ estimated from batch least-squares inversions of CO₂ concentration measurements, Ph.D. thesis, Princeton Univ., Princeton, N. J.
- Bakwin, P. S., P. P. Tans, C. Zhao, W. Ussler, and E. Quesnell (1995), Measurements of carbon dioxide on a very tall tower, *Tellus*, *37B*, 535–549.
- Bakwin, P. S., P. P. Tans, D. F. Hurst, and C. Zhao (1998), Measurements of carbon dioxide on very tall towers: Results of the NOAA/CMDL program, *Tellus*, *50B*, 401–415.

- Battle, M., M. L. Bender, P. P. Tans, J. W. C. White, J. T. Ellis, T. Conway, and R. J. Francey (2000), Global carbon sinks and their variability inferred from atmospheric O₂ and δ¹³C, *Science*, *287*, 2467–2470.
- Bender, M., T. Ellis, P. P. Tans, R. Francey, and D. Lowe (1996), Variability in the O₂/N₂ ratio of southern hemisphere air, 1991–1994: Implications for the carbon cycle, *Global Biogeochem. Cycles*, *10*, 9–21.
- Blackadar, A. K. (1976), Modeling nocturnal boundary layer, paper presented at Third Symposium on Atmospheric Turbulence Diffusion and Air Quality, Am. Meteorol. Soc., Reno, Nev.
- Blackadar, A. K. (1978), Modeling pollutant transfer during daytime convection, paper presented at Fourth Symposium on Atmospheric Turbulence Diffusion and Air Quality, Am. Meteorol. Soc., Reno, Nev.
- Bousquet, P., P. Ciais, P. Peylin, M. Ramonet, and P. Monfray (1999), Inverse modeling of annual atmospheric CO₂ sources and sinks: 1. Method and control inversion, *J. Geophys. Res.*, *104*, 26,161–26,178.
- Bousquet, P., P. Peylin, P. Ciais, C. L. Quere, P. Friedlingstein, and P. P. Tans (2000), Regional changes in carbon dioxide fluxes of land and oceans since 1980, *Science*, *290*, 1342–1346.
- Brown, S. (1996), Impacts adaptations and mitigation of climate change: Scientific-technical analyses, in *Climate Change 1995*, edited by R. T. Watson et al., pp. 773–797, Cambridge Univ. Press, New York.
- Brown, S. L., and P. E. Schroeder (1999), Spatial patterns of aboveground production and mortality of woody biomass for eastern US forests, *Ecol. Appl.*, *9*, 968–980.
- Businger, J. A., J. C. Wyngaard, Y. Izumi, and E. F. Bradley (1971), Flux profile relationships in the atmospheric surface layer, *J. Atmos. Sci.*, *28*, 181–189.
- Chen, J. M., J. Liu, J. Cihlar, and M. L. Guolden (1999), Daily canopy photosynthesis model through temporal and spatial scaling for remote sensing applications, *Ecol. Model.*, *124*, 99–119.
- Chen, J. M., et al. (2002), Validation of Canada-wide leaf area index maps using ground measurements and high and moderate resolution satellite imagery, *Remote Sens. Environ.*, *80*, 165–184.
- Ciais, P., P. P. Tans, M. Trolier, J. W. C. White, and R. J. Francey (1995), A large northern-hemisphere terrestrial CO₂ sink indicated by the ¹³C/¹²C ratio of atmospheric CO₂, *Science*, *269*, 1098–1102.
- Denning, A. S., I. Y. Fung, and D. A. Randall (1995), Latitudinal gradient of atmospheric CO₂ due to seasonal exchange with land biota, *Nature*, *376*, 240–243.
- Denning, A. S., G. J. Collatz, C. Zhang, D. A. Randall, J. A. Berry, P. J. Sellers, G. D. Colello, and D. A. Dazlich (1996a), Simulations of terrestrial carbon metabolism and atmospheric CO₂ in a general circulation model. Part 1: Surface carbon fluxes, *Tellus*, *48B*, 521–542.
- Denning, A. S., G. J. Collatz, C. Zhang, D. A. Randall, J. A. Berry, P. J. Sellers, G. D. Colello, and D. A. Dazlich (1996b), Simulations of terrestrial carbon metabolism and atmospheric CO₂ in a general circulation model. Part 2: Simulated CO₂ concentrations, *Tellus*, *48B*, 543–567.
- Denning, A. S., T. Takahashi, and P. Friedlingstein (1999), Can a strong atmospheric CO₂ rectifier effect be reconciled with a “reasonable” carbon budget?, *Tellus*, *51B*, 250–253.
- Dixon, R. K., et al. (1990), Carbon pools and flux of global forest ecosystems, *Science*, *263*, 185–190.
- Driedonks, A. G. M., and P. G. Duynkerke (1989), Current problems in the stratocumulus-topped boundary layer, *Boundary Layer Meteorol.*, *46*, 275–303.
- Enting, I. G., C. M. Trudinger, and R. J. Francey (1995), A synthesis inversion of the concentration and [delta]¹³C of atmospheric CO₂, *Tellus*, *47B*, 35–52.
- Esoque, M. A. (1968), Vertical mixing due to penetrative convection, *J. Atmos. Sci.*, *25*, 1046–1051.
- Fan, S., M. Gloor, J. Mahlman, S. Pacala, J. Sarmiento, T. Takahashi, and P. P. Tans (1998), A large terrestrial carbon sink in North America implied by atmospheric and oceanic carbon dioxide data and models, *Science*, *282*, 442–446.
- Garrett, A. J. (1981), Comparison of observed mixed-layer depths to model estimates using observed temperatures and winds, and MOS forecasts, *J. Appl. Meteorol.*, *20*, 1277–1283.
- Gurney, R. K. (2002), Towards robust regional estimates of CO₂ sources and sinks using atmospheric transport models, *Nature*, *415*, 626–630.
- Heimann, M. (2001), The carbon cycle and atmospheric CO₂, in *Atmospheric Inversion Calculations Performed for IPCC Third Assessment Report*, chap. 3, Max-Planck-Inst. für Biogeochem., Jena, Germany.
- Higuchi, K., D. Worthy, D. Chan, and A. Shashkov (2003), Regional source/sink impact on the diurnal, seasonal and inter-annual variations in atmospheric CO₂ at a boreal forest site in Canada, *Tellus, Ser. B.*, *55*, 115–125.
- Hollinger, D. Y., F. M. Kelliher, J. N. Byers, J. E. Hunt, T. M. Sevensy, and P. L. Weir (1994), Carbon dioxide exchange between an undisturbed old growth temperate forest and the atmosphere, *Ecology*, *75*, 134–150.
- Holtslag, A. A. M., and B. A. Boville (1993), Local versus nonlocal boundary-layer diffusion in a global climate model, *J. Clim.*, *6*, 1825–1842.
- Holtslag, A. A. M., and C. H. Moeng (1991), Eddy diffusivity and countergradient transport in the convective atmospheric boundary layer, *J. Atmos. Sci.*, *48*, 1690–1698.
- Houghton, R. A., J. L. Hachler, and K. T. Lawrence (1999), The U.S. carbon budget: Contributions from land-use change, *Science*, *285*, 574–578.
- Kaminski, T., M. Heimann, and R. Giering (1999), A coarse grid three-dimensional global inverse model of the atmospheric transport: 2. Inversion of the transport of CO₂ in the 1980s, *J. Geophys. Res.*, *104*, 18,555–18,581.
- Keeling, C. D., R. B. Bacastow, A. F. Carter, S. C. Piper, T. P. Whorf, M. Heimann, W. G. Mook, and H. Roeloffzen (1989), A three-dimensional model of atmospheric CO₂ transport based on observed winds. 1: Analysis of observed data, in *Aspects of Climate Variability in the Pacific and Western Americas*, *Geophys. Monogr. Ser.*, vol. 55, edited by D. H. Peterson, pp. 165–236, AGU, Washington, D. C.
- Keeling, R. F., S. C. Piper, and M. Heimann (1996), Global and hemispheric CO₂ sinks deduced from changes in atmospheric O₂ concentration, *Nature*, *381*, 218–221.
- Kurz, W. A., and M. J. Apps (1999), A 70 year retrospective analysis of carbon fluxes in the Canadian forest sector, *Ecol. Appl.*, *9*, 526–547.
- Lee, X. (1998), On micrometeorological observations of surface-air exchange over tall vegetation, *Agric. For. Meteorol.*, *91*, 39–49.
- Lee, X., and X. Hu (2002), Forest-air fluxes of carbon, water and energy over non-flat terrain, *Boundary Layer Meteorol.*, *103*, 277–301.
- Lee, X., O. R. Bullock Jr., and R. J. Andres (2001), Anthropogenic emission of mercury to the atmosphere in the northeast United States, *Geophys. Res. Lett.*, *28*, 1231–1234.
- Liu, J., J. M. Chen, J. Cihlar, and W. Chen (1999), Net primary productivity distribution in BOREAS region from a process model using satellite and surface data, *J. Geophys. Res.*, *104*, 27,735–27,754.
- Liu, J., J. M. Chen, J. Cihlar, and W. Chen (2002), Net primary productivity mapped for Canada at 1-km resolution, *Global Ecol. Biogeogr.*, *11*, 115–129.
- McGuire, A. D. (2001), Carbon balance of the terrestrial biosphere in the twentieth century: Analyses of CO₂, climate and land-use effects with four process-based ecosystem models, *Global Biogeochem. Cycles*, *15*, 183–206.
- McMillen, R. T. (1988), An eddy-correlation technique with extended applicability to non-simple terrain, *Boundary Layer Meteorol.*, *43*, 231–245.
- Pacala, S. W., et al. (2001), Consistent land- and atmospheric-based US carbon sink estimates, *Science*, *292*, 2316–2320.
- Pandolfo, J. P. (1966), Wind and temperature profiles for constant-flux boundary layers in lapse conditions with a variable eddy conductivity to eddy viscosity ratio, *J. Atmos. Sci.*, *23*, 495–502.
- Paw, U. K. T., D. D. Baldocchi, T. P. Meyers, and K. B. Wilson (2000), Correction of eddy-covariance measurements incorporating both advective effects and density fluxes, *Boundary Layer Meteorol.*, *97*, 487–511.
- Pearman, G. I., and P. Hyson (1980), Activities of the global biosphere as reflected in atmospheric CO₂ records, *J. Geophys. Res.*, *85*, 4468–4474.
- Potter, C. S., J. T. Randerson, C. B. Field, P. A. Matson, P. M. Vitousek, H. A. Mooney, and S. A. Klooster (1993), Terrestrial ecosystem production: A process model based on global satellite and surface data, *Global Biogeochem. Cycles*, *7*, 811–841.
- Prentice, I. C., et al. (2001), The scientific basis, in *Climate Change 2001*, edited by J. T. Houghton and D. Yihui, pp. 183–237, chap. 3, Cambridge Univ. Press, New York.
- Rayner, P. J., I. G. Enting, R. J. Francey, and R. Langenfelds (1999), Reconstructing the recent carbon cycle from atmospheric CO₂, [delta]¹³C and O₂/N₂ observations, *Tellus*, *51B*, 213–232.
- Running, S. W., D. D. Baldocchi, D. P. Turner, S. T. Gower, P. S. Bakwin, and K. A. Hibbard (1999), A global terrestrial monitoring network integrating tower fluxes, flask sampling, ecosystem modeling and EOS satellite data, *Remote Sens. Environ.*, *70*, 108–127.
- Schimel, D., et al. (2000), Contribution of increasing CO₂ and climate to carbon storage by ecosystems in the United States, *Science*, *287*, 2004–2006.
- Schimel, D. S., et al. (2001), Recent patterns and mechanisms of carbon exchange by terrestrial ecosystems, *Nature*, *414*, 169–172.
- SENEC (1997), A mixing height study for North America (1987–1991), report, Richmond Hill, Ontario, Canada.
- Spiecker, H., K. Mielikäinen, M. Köhl, and J. P. Skovsgaard (1996), *Growth Trends in European Forests*, Springer-Verlag, New York.
- Stephens, B. B. (1999), Field-based atmospheric O₂ measurements and the ocean carbon cycle, Ph.D. thesis, 221 pp., Scripps Inst. of Oceanogr., La Jolla, Calif.

- Stephens, B. B., R. F. Keeling, P. P. Tan, M. Heimann, K. D. Six, R. Murnane, and K. Calderira (1998), Testing global ocean carbon cycle models using measurements of atmospheric O₂ and CO₂ concentration, *Global Biogeochem. Cycles*, *12*, 213–230.
- Stephens, B. B., S. C. Wofsy, R. F. Keeling, P. P. Tan, and M. J. Potosnak (2000), The O₂ budget and rectification airborne study: Strategies for measuring rectifiers and regional, in *Inverse Methods in Global Biogeochemical Cycles*, *Geophys. Monogr. Ser.*, vol. 114, edited by P. Kasibhatla et al., pp. 311–324, AGU, Washington, D. C.
- Stull, R. B. (1993), *An Introduction to Boundary Layer Meteorology*, Kluwer Acad., Norwell, Mass.
- Taguchi, S. (2000), Synthesis inversion of atmospheric CO₂ using the NIRE chemical transport model, in *Inverse Methods in Global Biogeochemical Cycles*, *Geophys. Monogr. Ser.*, vol. 114, edited by P. Kasibhatla et al., pp. 239–254, AGU, Washington, D. C.
- Tans, P. P., I. Y. Fung, and T. Takahashi (1990), Observation constraints on the global atmospheric CO₂ budget, *Science*, *247*, 1431–1438.
- Verma, S. B., D. D. Baldocchi, D. E. Anderson, D. R. Matt, and R. J. Clement (1986), Eddy fluxes of CO₂, water vapor, and sensible heat over a deciduous forest, *Boundary Layer Meteorol.*, *36*, 71–91.
- Westphal, D. L. (1981), The interaction between radiative and boundary layer processes in stratus clouds, M.S. thesis, 138 pp., Penn. State Univ., University Park, Penn.
- Yi, C., K. J. Davis, P. S. Bakwin, B. W. Berger, and L. C. Marr (2000), Influence of advection on measurements of the net ecosystem-atmosphere exchange of CO₂ from a very tall tower, *J. Geophys. Res.*, *105*, 9991–9999.
- Yi, C., K. J. Davis, and B. W. Berger (2001), Long-term observations of the dynamics of the continental planetary boundary layer, *J. Atmos. Sci.*, *58*, 1288–1299.
- Zeman, O. (1977), Parameterization of the turbulent energy budget at the top of the daytime atmospheric boundary layer, *J. Atmos. Sci.*, *34*, 111–123.
- Zhang, D., and R. Anthes (1982), A high-resolution model of the planetary boundary layer-sensitivity tests and comparisons with SESAME-79 data, *J. Appl. Meteorol.*, *21*, 1594–1608.
-
- D. Chan, K. Higuchi, and A. Shashkov, Air Quality Research Branch, Meteorological Service of Canada, 4905 Dufferin Street, Toronto, Ontario, Canada M3H 5T4. (douglas.chan@ec.gc.ca; kaz.higuchi@ec.gc.ca; alexander.shashkov@ec.gc.ca)
- B. Chen and J. M. Chen, Department of Geography and Program in Planning, University of Toronto, 100 St. George Street, Room 5047, Toronto, Ontario, Canada M5S 3G3. (chenj@geog.utoronto.ca)
- J. Liu, Department of Physics, University of Toronto, 60 St. George Street, Toronto, Ontario, Canada M5S 1A7. (jliu@atmosph.physics.utoronto.ca)

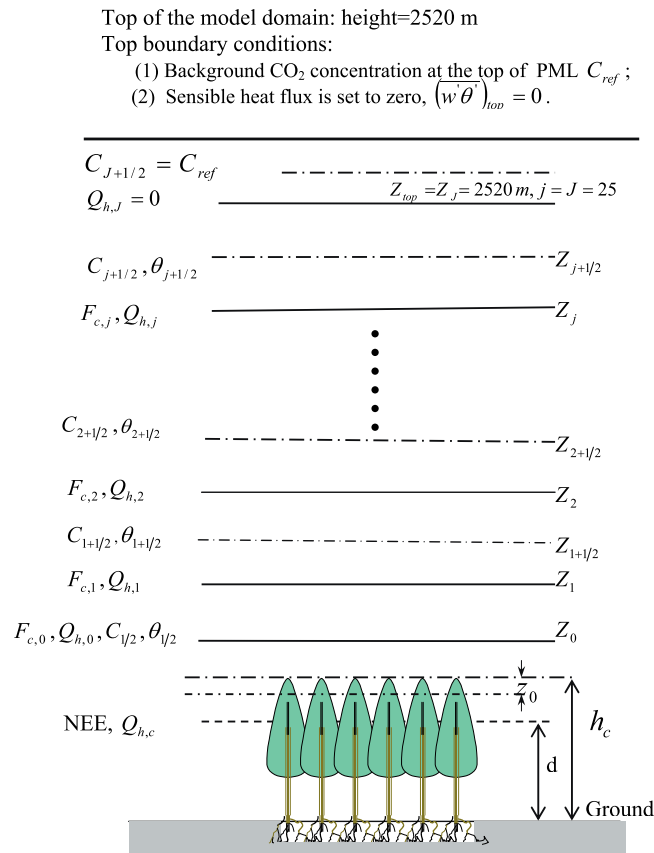


Figure 2. Schematic vertical structure of the VDS model domain (h_c is the height of the vegetation canopy, d is the displacement height, z_0 is the roughness length, C is the CO₂ concentration, θ is the potential temperature of air; F is the CO₂ flux; and Q_h is the sensible heat flux. The subscripts “0” and “1/2” denotes the lower surface layer for the CO₂ flux and the sensible heat flux, and for the CO₂ concentration and the potential temperature of air, respectively. Here j is each layer with a vertical separation of 100 m, J - is the top of model domain (= 25)).